CRYSTAL BARREL TECHNICAL REPORT
CBNOTE 308

# Rare radiative $\omega$ decays ($\omega \to \eta\gamma$ and $\omega \to 3\gamma$)

Claudio Pietra
Universität Zürich

CERN, Genève, August 1996

# Abstract

Antiproton-proton annihilation at rest into $\pi^0\omega$ and $\eta\omega$ was used to study radiative decays of the $\omega$ meson, in particular to determine the branching ratio $BR(\omega \to \eta\gamma)$ and to search for the direct decay $\omega \to 3\gamma$. Out of 15.5M $\overline{p}p$ annihilations into final states with no charged particles, 63k $\pi^0\omega$ and 55k $\eta\omega$ events were reconstructed requiring $\pi^0, \eta \to 2\gamma$ and $\omega \to 3\gamma$. The resulting $\omega \to 3\gamma$ Dalitz plots were analysed.

From the channel $\overline{p}p \to \eta\omega$, the branching ratio $BR(\omega \to \eta\gamma)$ was measured by assuming no coherent contribution from $\rho$:

$$BR(\omega \to \eta\gamma)_{\eta\omega} \;=\; (7.05 \pm 1.19) \times 10^{-4}.$$

The corresponding branching ratio measured in $\pi^0\omega$ ($(14.7 \pm 4.6) \times 10^{-4}$) is a factor of 2 larger due to the strong coherent contribution from $\overline{p}p \to \pi^0\rho, \rho \to \eta\gamma$. The coherent admixture from $\rho$ can therefore not be neglected, at least in the $\pi^0\omega$ channel.

To gain information on the sign of $\rho - \omega$ interference, and to prove that the coherent contribution from $\rho$ can be neglected in the $\eta\omega$ channel, a coupled analysis of both $\omega$ production channels was performed. The $\rho$ contribution was simulated using Monte Carlo events. The final results are:

$$\begin{aligned} BR(\omega \to \eta\gamma)_{\pi^0\omega,\eta\omega} &= (6.6 \pm 1.7) \times 10^{-4}, \\ \phi_{\rho-\omega} &= (-18^{+58}_{-27})^\circ. \end{aligned}$$

The relative phase $\phi$ between $\rho$ and $\omega$ is therefore consistent with zero (constructive interference). No ambiguities between constructive and destructive interference were found. The coupled analysis furthermore determines the branching ratio $BR(\rho \to \eta\gamma) = (9.1 \pm 6.8) \times 10^{-4}$ with very large errors.

In addition, an upper-limit for the direct radiative decay $\omega \to 3\gamma$ (without intermediate resonances) was measured in the $\pi^0\omega$ channel:

$$BR(\omega \to 3\gamma) < 1.9 \times 10^{-4} \text{ at } 95\%\ CL.$$

# Contents


**1 Introduction** **2**

**2 The Crystal Barrel Detector** **4**
2.1 The Crystal Calorimeter . . . . . 4

**3 Data Reconstruction and Offline Analysis** **7**
3.1 PED Reconstruction . . . . . 7
3.2 Split-Off Recognition . . . . . 8
3.3 Kinematic Fitting . . . . . 10

**4 Data Selection** **12**
4.1 Selection of events with 5 PED's and 0 tracks . . . . . 12
4.2 Selection of $\pi^0\omega$ and $\eta\omega$ Events . . . . . 14

**5 Monte Carlo Simulations** **22**
5.1 Background Simulation of Events with 6 $\gamma$'s . . . . . 22
5.2 Background Simulation of Events with 5 $\gamma$'s . . . . . 27
5.3 Reconstruction Efficiencies of $\pi^0\omega$ and $\eta\omega$ . . . . . 29

**6 Analysis** **30**
6.1 The $\eta\omega$ Channel . . . . . 30
6.2 The $\pi^0\omega$ Channel . . . . . 36
6.3 Upper Limit for the Branching Ratio $\omega \to 3\gamma$ . . . . . 40
6.4 $\rho - \omega$ Mixing . . . . . 43
6.4.1 Theory of $\rho - \omega$ Mixing . . . . . 43
6.4.2 Coupled Analysis of Both Channels . . . . . 46

**7 Discussion** **53**

**8 Conclusions** **55**

**A The Kinematic Fitting Method** **57**

**B The Normalization of 6$\gamma$ Background Channels** **59**

**C Errors on Weighted Histograms** **62**

# 1 Introduction

In the quark model [1], mesons are bound states of a quark and an antiquark. With three flavors of quarks, $(u, d, s)$, there are nine possible $q\overline{q}$ combinations for given spin and parity. The resulting multiplet structure is usually described by 'flavour $SU(3)$' symmetry. Since the masses of $(u, d)$ and $s$ quarks are different, $SU(3)_f$ is not an exact symmetry. However, even in the absence of knowledge about the potential which binds the quark to the antiquark, the model is very *predictive*. Many decay amplitudes and masses can be calculated using $SU(3)$ [2].

In QCD (quantum chromodynamics), the field theory of strong interactions, the coupling constant $\alpha_s$ increases with distance between the quarks, due to the self-coupling of gluons which themselves carry colour, the charge of the strong interaction. Thus only at very short distances ($< 0.1$ fm), equivalent to high energies, perturbation theory can be used. Calculations in the low energy region are therefore very difficult.

Thus $SU(3)$ is still used to classify and explain the spectrum of mesons, despite that the symmetry is not exact. $SU(3)$ is used particularly to determine the content of new mesons and assign them to $q\overline{q}$ nonets. If the decay modes of a meson is not compatible with $SU(3)$, it is possible that this meson is not a $q\overline{q}$ state but a hybrid or glueball (see, for instance, ref. [3] for an the interpretation of $f_0(1500)$ as the scalar groundstate glueball). It is therefore crucial for the understanding of the strong interaction at low energy to test the quark model and its extensions.

Radiative decays of light mesons provide a good testing of the quark model since radiative decay amplitudes can be calculated reliably [4]. The calculation of the decay width for $\omega \to \pi^0\gamma$ was one of the first triumphs of the quark model in the mid-sixties.

On the other hand, the experimental situation is not very satisfying. Many radiative decay amplitudes are not well-known or different experiments measure incompatible values. In particular, the sign of the interference of the two mesons $\omega$ and $\rho$ has not yet been unambigously determined.

The aim of this analysis is to improve the measurement of radiative decays of the $\omega$ meson, to solve the open problem of $\rho-\omega$ mixing and to search for the direct decay $\omega \to 3\gamma$. Since the decay $\omega \to \pi^0\gamma$ is already well-known, special emphasis was put on the decay $\omega \to \eta\gamma$. Only one experiment claims to have measured this decay amplitude in a 'model independent' way [5], while other experiments obtain equailly good solutions for constructive and destructive $\rho - \omega$ mixing [6] [7]. So far, no experiment could unambiguously determine the relative phase. However, constructive interference is much favoured by the 'model independent' measurement and by the quark model.

The Crystal Barrel experiment [8] [9] at CERN, which studies proton-antiproton annihilation at rest and in-flight, is specially well suited to measure radiative decays of light mesons because of its $4\pi$ electromagnetic calorimeter. In this work, the reactions $\overline{p}p \to \pi^0\omega \to 5\gamma$ and $\overline{p}p \to \eta\omega \to 5\gamma$ were used as a source

of $\omega$ mesons. The analysis required 5 detected photons in the crystal calorimeter and no charged particles in the drift chambers. The $\omega$ mesons were reconstructed with a kinematic fit and the $\omega \to 3\gamma$ Dalitz plot was analysed.

The open problem about the sign of $\rho - \omega$ interference is solved in the present work. Since two different production channels for the $\omega$ mesons are analysed, and hence two different the relative contributions from $\rho$, the sign of $\rho - \omega$ interference can be determined unambiguously by comparing of the two channels $\pi^0\omega$ and $\eta\omega$.

# 2 The Crystal Barrel Detector

The Crystal Barrel experiment at the low energy antiproton ring (LEAR) at CERN was designed to study meson spectroscopy. It was proposed in 1985 [8] and came into operation in 1989. It is presently located on beam line C2 at LEAR.

Its main purpose is to investigate $\overline{p}p$ annihilation at rest. The central issue is to search for glueballs and hybrids decaying into neutral mesons such as $\pi^0$'s, $\eta$'s and $K$'s. A second goal is to measure radiative and rare decays of well known mesons. For these two issues, special emphasis has to be put on photon detection. But, since only about 4% of all $\overline{p}p$ annihilations have no charged particles in the final state, an efficient tracking and trigger on charged multiplicity is also crucial for the identification of charged $\pi$'s and $K$'s.

A detailed description of the apparatus can be found in ref. [9]. The overall layout of the detector is shown in figure 1. Antiprotons of 200 MeV/$c$ are extracted from LEAR for annihilation at rest. They stop in a target (6) filled with liquid hydrogen and form protonium which annihilates mainly from $S$ states. The target is surrounded by two proportional wire chambers (PWC's) (5) which give the first measurement of charged particles close to the interaction vertex and serve as fast charged multiplicity trigger. The wires of the inner chamber are at a radius of 25.5 mm from the beam axis while those of the outer chamber are at a radius of 43 mm. The inner chamber covers 99%, the outer chamber 97% of the full solid angle. The total detection efficiency for charged particles exceeds 99%. Leaving the proportional chambers, a particle enters the jet drift chamber (JDC) (4) with 30 azimuthal sectors and 23 radial layers which give the $r\phi$ coordinates as well as the $z$ position along the beam direction through charge division. The innermost wires of the JDC are at a radius of 63 mm, the outermost at 239 mm. An electromagnetic calorimeter of $CsI(Tl)$ crystals (3) surrounds the drift chamber and measures the energy deposit of photons and charged particles. All subdetectors are inside a magnetic coil which produces a uniform magnetic field of 1.5 T along the beam axis.

The present work is based on all neutral triggered events (e.g. final states with no charged particles), for which the the measurement of photons in the calorimeter is essential. The two PWC's and the JDC are only used to veto charged particles.

## 2.1 The Crystal Calorimeter

Photons with energies from 10 MeV to 2000 MeV can be measured in the electromagnetic calorimeter consisting of 1380 $CsI(Tl)$ crystals of 30 cm length (16 radiation length) each. The geometrical cross section of the crystals is that of a trapezoid. They are arranged in 26 rings pointing to the interaction region. Each crystal is a separate unit enclosed in a 0.1 mm thick titanium can. The calorimeter covers polar angles $\theta$ between 12° and 168° with full coverage in azimuthal angle $\phi$. Each crystal covers 6° in $\theta$ and 6° in $\phi$, except for the last 3

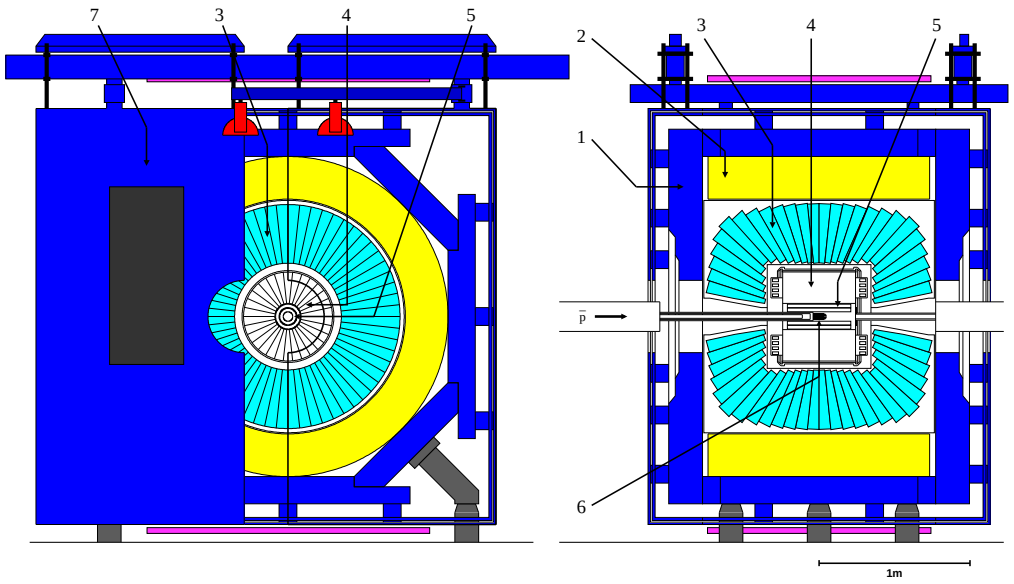


Figure 1: *The Crystal Barrel detector. (1) magnet yoke, (2) magnet coils, (3) CsI barrel, (4) jet drift chamber (JDC), (5) proportional chambers (PWC's), (6) liquid hydrogen target, (7) one-half of the endplate.*

rows of crystals near the beam axis ($\theta < 15°$ and $\theta > 168°$) where $\Delta\phi$ had to be increased to 12°.

Since the whole detector is located in a strong magnetic field, the crystals are read out silicon photodiodes glued to the edge of a wavelength shifter plate The $CsI$ emission spectrum, which peaks at 550 nm, and the absorbtion spectrum of the wavelength shifter, consisting of a plexiglas tile doped with an optically active pigment, are well matched and the quantum efficiency of the photodiode is around 80% in the emission range of the wavelength shifter. The employment of a wavelength shifter ensures a high light collection efficiency by the photodiode. An arrangement without wavelength shifter would require several photodiodes to cover the back end of a crystal in order to absorb most of the light. The luminescene signal of the $CsI$ is reflected in the photodiode signal which has about 40 ns risetime and decays over several $\mu$s. A preamplifier, mounted behind the photodiode, integrates and amplifies the signal after which a differential driver sends it over a twisted-pair cable of 18 m length to the main electronics hut. In the hut, the signal is again amplified and shaped into an approximate gaussian, divided into two outputs and finally fed into two charge integrating ADC systems. One (LeCroy 2282) covers the energy range between 0 and 400 MeV, whereas the other (LeCroy Fera) covers the full range from 0 to 2000 MeV. The Fera ADC's have a fast conversion time of 9 $\mu$s and can be used in a height level software

trigger.

Before the calorimeter was assembled each crystal module was pre-calibrated with 6.1 MeV photons from a $Pu^{13}C$ source. The final calibration (the method which yields the highest energy resolution) is done the following way: events with several photons are used to to find a $\pi^0$ invariant mass peak. The calibrations constants for each crystal can now be adjusted until the $\pi^0$ has the required mass. The energy resolution of a photon after the calibration is

$$\frac{\sigma(E_\gamma)}{E_\gamma} = \frac{2.5\%}{\sqrt[4]{E\ [\mathrm{GeV}]}}. \tag{1}$$

The spatial resolution is also energy-dependent and typically 25 mrad in $\theta$ and $\phi$.

# 3 Data Reconstruction and Offline Analysis

The identification of charged and neutral particles and the reconstruction of their energy and momenta is done by an offline analysis package *(CBOFF)*, which has been developed during the past years. The whole software is written in *Fortran 77*. The user can provide several analysis and selection routines to obtain his own analytical software.

This work is based on *zero-prong* triggered events (events with no charged particles in the PWC and JDC). Of particular interest in this case is the reconstruction of energy deposits in the calorimeter and the assignment of these Particle Energy Deposits (PED's) to photons. The JDC and PWC data are only used to veto residual charged tracks.

## 3.1 PED Reconstruction

A photon which is absorbed in the crystal calorimeter induces an electromagnetic shower, a cascade of secondary photons, electrons and positrons. Due to the statistical nature of this process, the shower is not restricted to one crystal but spreads over several neighbouring crystals. The primary photon therefore deposits its energy in several neighbouring crystals. Such a cluster of crystals can reach up to 20 crystals. Each crystal measures the energy deposit through the scintillator effect. The aim of the reconstruction algorithm is to assign such a cluster of crystals to a photon and extract the energy as well as $\theta$ and $\phi$.

The user can set two values for the reconstruction:

- *ECLUBC*: Minimal energy in MeV for the sum over neighbouring crystals to generate a *cluster*, typically between 4 and 20 MeV.
- *EPEDBC*: Minimal energy in MeV for a single crystal to count as a *Particle Energy Deposit* (PED), typically between 10 and 20 MeV.

The algorithm performs the reconstruction in several steps. First, clusters of neighbouring crystals with energy deposits above 1 MeV are searched for. Local maxima are then searched for within the clusters which have energies greater than *ECLUBC*.

1. When only one maximum is found within the cluster, the photon energy is then defined as being the total energy deposit in the cluster. The direction of the photon is given by the energy-weighted angles of the crystals in the cluster.

2. When two or more local maxima are found in the same cluster, it is assumed that the cluster originates from more than one photon. The total cluster energy is therefore divided between the photons. Each local maxima exceeding the value *EPEDBC*, together with its eight neighbouring crystals, is defined as a subcluster. Let us define

$$\begin{aligned} n &: \text{Number of subclusters} \\ E_{cluster} &: \text{Total energy of the parent cluster} \\ E_{9,i} &: \text{Energy of a subcluster } i. \end{aligned} \tag{2}$$

The energy of the photon associated with the subcluster $j$ is given then by

$$E_{\gamma,j} = \frac{E_{9,j}}{\sum_{i=1}^{n} E_{9,i}} \cdot E_{cluster}. \tag{3}$$

Such a reconstructed photon is called *PED* (particle energy deposit). With this method, the energy of the cluster is shared among the $n$ PED's so that

$$\sum_{i=1}^{n} E_{\gamma,i} = E_{cluster}. \tag{4}$$

The number of reconstructed PED's depends strongly on the two values provided by the user, *ECLUBC* and *EPEDBC*. The higher these two parameters are, the more $\gamma$'s fall below the energy threshold and are not reconstructed by the offline program. The lower these parameters are, the more PED's are found which might originate from real $\gamma$'s but also from electromagnetic fluctuations (so called *split-off*'s, see section 3.2). The optimum set of parameters depends on the type of analysis. The calibration method for the crystal calorimeter and the energy resolution for a photon is discussed in section 2.1.

## 3.2 Split-Off Recognition

Secondary photons from the electromagnetic shower in the calorimeter can travel more than one crystal without interactions. These photons deposit their energy several crystals away from the impact point of the primary photon. The algorithm described in section 3.1 associates these energy deposits to additional photons. Such a *split-off* PED lies near the parent PED and has in general a lower energy. One therefore defines

$$\begin{aligned} \cos\phi_{ij} &= \frac{\vec{p}_i \cdot \vec{p}_j}{|\vec{p}_i|\,|\vec{p}_j|}, \\ R_{ij} &= \frac{E_i}{E_j} \leq 1, \end{aligned} \tag{5}$$

where the indices $i$ and $j$ run through all PED's, $i \neq j$. The variables $\cos\phi_{ij}$ vs. $R_{ij}$ are plotted in figure 2 for a subsample of the 5 PED data sample. The enhancement visible in the upper left corner at low $\phi_{ij}$ and $R_{ij}$ is due to *split-off* events. The band at $\cos\phi_{ij} \simeq 0.9$ originates from $\pi^0 \to 2\gamma$, where the $\pi^0$ decays through the minimum opening angle. For $\pi^0$'s, a low ratio $E_{\gamma_1}/E_{\gamma_2}$ corresponds to a large opening angle and an angle near $0^\circ$ is not possible[1]. This feature is used for a sophisticated cut on split-off events.

[1]The $\eta$'s decaying into 2 $\gamma$'s do not appear in the region where $\cos\phi_{ij} \approx 1$ since the low kinetic energy of the $\eta$'s does not permit such a small opening angle.

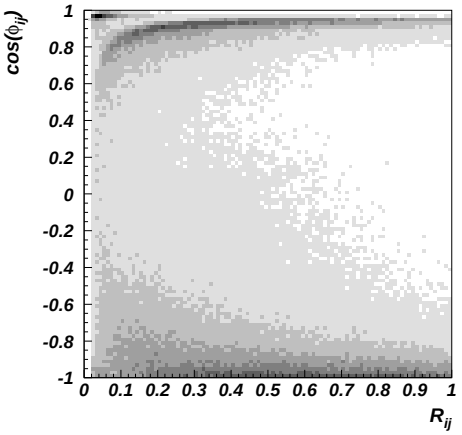


Figure 2: $\cos\phi_{ij}$ *vs.* $R_{ij}$ *for a subsample of the 5 PED data sample. An enhancement is visible at very large* $\cos\phi_{ij}$ *and small energy ratios* $R_{ij}$ *due to split-off events.*

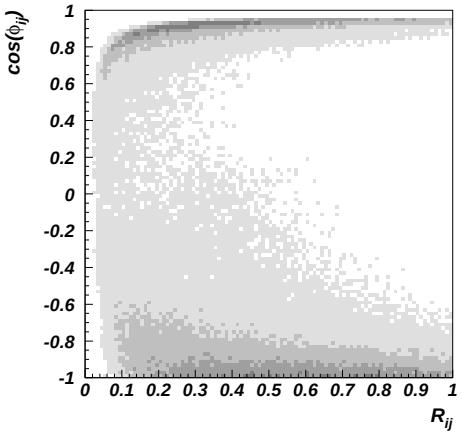


Figure 3: *Same as in figure 2, but after the split-off cut.*

Assume a $\pi^0$ with total energy $E_{\pi^0} = \gamma \cdot m_{\pi^0}$ decaying into two $\gamma$'s with energies $E_1$, $E_2$. The $\pi^0$ mass is given by

$$\begin{aligned} m_{\pi^0}^2 &= (E_1 + E_2)^2 - (\vec{p}_1 + \vec{p}_2)^2 \\ &= E_1^2 + E_2^2 + 2E_1E_2 - \vec{p}_1^{\,2} - \vec{p}_2^{\,2} - 2\vec{p}_1\vec{p}_2. \\ &= 2E_1E_2(1 - \cos\phi), \end{aligned} \tag{6}$$

where $\phi$ is the opening angle. Solving equation 5 for $\cos\phi$, one finds:

$$\begin{aligned} \cos\phi &= \frac{2E_1E_2 - m^2}{2E_1E_2} \\ &= 1 - \frac{E_1^2 + E_2^2 + 2E_1E_2}{2\gamma^2 E_1E_2} \\ &= 1 - \frac{R^2 + 2R + 1}{2\gamma^2 R} \\ &= 1 - \frac{(1+R)^2}{2\gamma^2 R}. \end{aligned} \tag{7}$$

Split-off events show a systematically larger $\cos\phi$ than two $\gamma$'s from $\pi^0$ decay and a cut on split-off events is therefore defined, rejecting events whenever

$$\cos\phi_{ij} > 1 - \frac{(1+R_{ij})^2}{2 \cdot \gamma_{limit}^2 \cdot R_{ij}} \tag{8}$$

occurs for at least one 2 PED combination $ij$. The value $\gamma_{limit}$ is the cut parameter, which has to be set significantly higher than the highest possible $\gamma$ in the reaction being analysed.

For the reaction $\overline{p}p \to \pi^0\omega$, which is dominant in the 5 PED final state, the maximum $\pi^0$ momentum is the one from $\omega \to \pi^0\gamma$ which has a maximum $\gamma_{\pi^0}$ of 6.92. In figure 3, $\cos\phi_{ij}$ vs. $R_{ij}$ is plotted after the cut for $\gamma_{limit} = 8$. The split-off events in the upper left region vanish completely, while the $\pi^0$ band is not affected.

## 3.3 Kinematic Fitting

Every measurement of physical quantities is, within the instrumental resolution, flawed with errors. A commonly used method to improve the measurement is to express physical relations between the quantities and vary them within the errors until all relations are satisfied. The necessary corrections to the measured variables should be as small as possible. Mathematically spoken, one has to deal with a minimization problem with several constraining equations, so called *constraints* [10].

In the present work, such a *fit* to the data is used to test several kinematic hypotheses such as $\overline{p}p \to \pi^0\omega$ or $\overline{p}p \to \eta\omega$ and to select events according to the goodness of the fit. The fit is done using the method of least squares minimization. A complete derivation of the fit method can be found in appendix A.

In the Crystal Barrel experiment, 3 variables are measured for each $\gamma$, namely $E$, $\theta$ and $\phi$. Hence for $m$ measured $\gamma$'s, one has $n = 3 \cdot m$ parameters. With $m_\gamma = 0$ one calculates the momentum for $\gamma_i$:

$$\begin{aligned} (p_x)_i &= E_i \sin\theta_i \cos\phi_i, \\ (p_y)_i &= E_i \sin\theta_i \sin\phi_i, \\ (p_z)_i &= E_i \cos\theta_i. \end{aligned} \tag{9}$$

For $\overline{p}p$ annihilation at rest, the total momentum has to be 0 whereas the total energy equals the mass of the protonium,

$$\begin{aligned} \textstyle\sum_{i=1}^{m} \vec{p}_i &= 0, \\ \textstyle\sum_{i=1}^{m} E_i &= 2 \cdot m_p, \end{aligned} \tag{10}$$

which already gives 4 constraining equations. To introduce a narrow resonance $R$ which decays into $\gamma$'s (e.q. a $\pi^0$ or $\omega$), further equations can be expressed in the form

$$\left(\sum_{k=1}^{N} E_i\right)^2 - \left(\sum_{k=1}^{N} \vec{p}_i\right)^2 = m_R^2, \tag{11}$$

where $m_R$ denotes the mass of the resonance and $N$ the number of $\gamma$'s to which $R$ decays. The sum over the $N$ $\gamma$'s has to be performed with all possible $\gamma$ combinations to test every assignment of the $\gamma$'s to $R$. The combination with the lowest $\chi^2$ is then chosen. Every introduction of a resonance adds one constraining equation. A fit with 6 constraints is called a 6C-fit.

The result of a kinematic fit can be judged by the outcoming $\chi^2$. The probability that the kinematics of a given event indeed corresponds to the tested

hypothesis equals the upper tail probability (integration from $\chi^2$ to $\infty$) of the $\chi^2$ distribution with $n_f = n - q$ ($q$: number of constraints) degrees of freedom. An event can therefore be kept (or thrown away) with a cut on this *confidence level*.

A method to check whether the fit results are correct is to look at the *pulls*:

$$\Delta x_i = \frac{x_i^0 - x_i}{\sqrt{\sigma_{x_i^0}^2 - \sigma_{x_i}^2}}. \tag{12}$$

If the detector resolution is well understood and the errors are correctly estimated, $\Delta x_i$ is gaussian distributed around 0 (with $\sigma = 1$).

# 4 Data Selection

The present analysis is based on data from $\overline{p}p$ annihilation into final states with no charged particles. The trigger on these zero-prong events uses the charged multiplicity from the two PWC's[2] to veto charged tracks. This leads to 15.5 Million triggered *all neutral* events from run periods December 1989, June, July and November 1990, May, June and August 1991. Table 1 summarizes the number of triggered all-neutral events on tape from the different run periods.

| Run Period | zero-prong events |
|---|---|
| December 1989 | 944,860 |
| June 1990 | 1,170,040 |
| July 1990 | 4,074,257 |
| November 1990 | 4,572,615 |
| May 1991 | 1,562,800 |
| July 1991 | 1,447,887 |
| August 1991 | 1,685,339 |
| Total | 15,457,788 |

Table 1: *Events used from initial DST tapes. No cuts have been applied.*

## 4.1 Selection of events with 5 PED's and 0 tracks

The method for the PED reconstruction was described in section 3.1. In order to find the optimum values for the energy cut levels EPEDBC and ECLUBC, the reconstruction efficiency for $\omega \to \eta\gamma$ events as well as the background contamination from $\pi^0\pi^0\eta$ in the $\pi^0\omega$ channel have been obtained by GEANT simulation (see chapter 5 for details on GEANT based Monte Carlo simulations) for different energy cut levels. The results are summarized in table 2. The reconstruction efficiency for $\omega \to \eta\gamma$ events is given in column 2, that for $\pi^0\pi^0\eta$ events in column 3. Both efficiencies drop with decreasing cut levels since more events are lost to higher multiplicities due to the split-off effect. The third row contains the signal to signal plus background ratio $S/(S+B)$. To calculate $S$ and $B$, one has to multiply the different production and decay branching ratios for $\overline{p}p \to \pi^0\omega, \omega \to \eta\gamma$ and $\overline{p}p \to \pi^0\pi^0\eta$ [11] [12] [13] with the reconstruction efficiencies obtained above.

The PED reconstruction with *EPEDBC/ECLUBC* = 20/20 MeV yields the highest reconstruction efficiency for $\omega \to \eta\gamma$ events, but background from $\pi^0\pi^0\eta$ is very strong so that the $S/(S+B)$ ratio is poor. For cut levels 10/10 MeV, the

[2]Except for the December 1989 and the June 1990 run, when the PWC's were not available yet. All neutral events from these run periods were obtained with a trigger in the inner layers of the JDC.

| EPEDBC / ECLUBC | $\varepsilon_{\omega\to\eta\gamma}$ | $\varepsilon_{\pi^0\pi^0\eta}$ | $S/(S+B)$ |
|---|---|---|---|
| 20 / 20 | 22.9 % | 0.180 % | 9 % |
| 10 / 10 | 16.5 % | 0.028 % | 32 % |
| 10 / 04 | 9.7 % | 0.019 % | 28 % |
| 04 / 04 | 4.0 % | 0.006 % | 35 % |

Table 2: *Scan for the optimum energy cut levels for the PED reconstruction.* $\varepsilon_{\omega\to\eta\gamma}$*: reconstruction efficiency for Monte Carlo* $\pi^0\omega, \omega \to \eta\gamma$ *events,* $\varepsilon_{\pi^0\pi^0\eta}$*: reconstruction efficiency for background events from* $\pi^0\pi^0\eta$*,* $S/(S+B)$*: signal to signal plus background ratio.*

reconstruction efficiency decreases slightly to 16.5%, but the background contamination decreases by a factor of 6, which improves the $S/(S+B)$ to 32%. For even lower cut levels, the reconstruction efficiency for $\omega \to \eta\gamma$ events decreases in the same manner as the background contamination, and hence the $S/(S+B)$ ratio does not improve any further. Thus for cut levels below 10/10, one only loses events without gaining a higher $S/(S+B)$ ratio.

The minimal energy for both PED's and clusters was therefore set to 10 MeV. Figure 4 and 5 show the distribution of PED's and tracks after reconstruction. The accumulations of events in figure 4 at 6 and 10 PED's are due to $\overline{p}p \to 3$ pseudoscalars and 5 pseudoscalars, respectively, where the pseudoscalars decay into $2\gamma$.

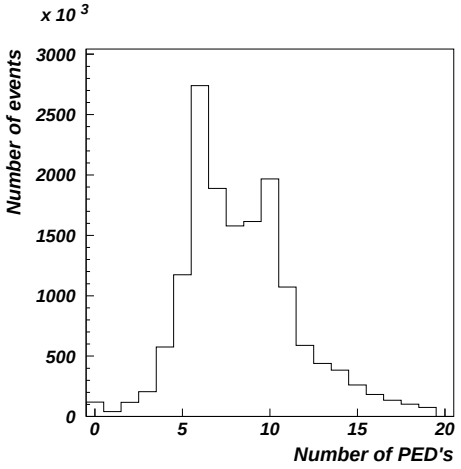


Figure 4: *Number of reconstructed PED's for zero-prong events.*

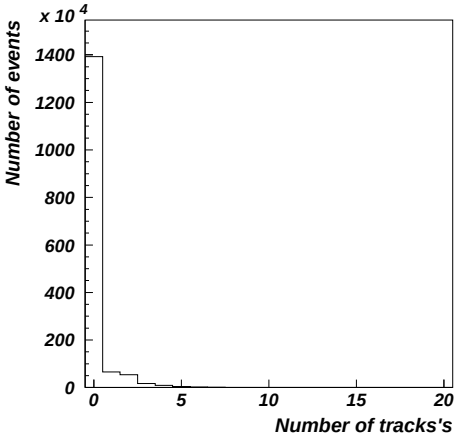


Figure 5: *Number of reconstructed tracks for zero-prong events.*

After the reconstruction, the following cuts were applied to the data:

- No charged tracks. The number of charged tracks was taken from the TTKS bank.

- Exactly 5 PED's.
- No split-off PED's. The cut used to reject events containing split-off's is described in section 3.2. The cut parameter $\gamma_{limit}$ was set to 8.

This gives a 5 PED data sample with about 1,173,000 events.

The figures on *p.* 15 show the general features of the 5 PED data sample. In figure 6, $E_{tot}$ vs. $p_{tot}$ is plotted for every event. The accumulation of events at $E_{tot} \simeq 2m_p = 1876$ MeV and $p_{tot} \simeq 0$ MeV/$c$ corresponds to events which are fully detected. The band is due to events for which one $\gamma$ escapes detection. For these events, the loss of energy equals the gain in total momentum.

For figures 7, 8 and 9, energy and momentum conservation of the 5 PED events is required by the following cuts:

$$\begin{array}{rl} 1800 < E_{tot}\ [\mathrm{MeV}] & < 2000, \\ 0 < p_{tot}\ [\mathrm{MeV}/c] & < 80. \end{array} \tag{13}$$

Note that these cuts were not applied in the analysis but only here to show the features of the 5 PED data sample.

In figure 7, $E_\gamma$ for all 5 photons is plotted. No narrow structures are observed. The 10 MeV cut on $\gamma$'s imposed by the PED reconstruction is clearly visible. In figures 8 and 9, the invariant mass of 2 and 3 $\gamma$'s is plotted. One clearly sees the lightest three mesons $\pi^0 \to 2\gamma$, $\eta \to 2\gamma$ and $\omega \to 3\gamma$.

## 4.2 Selection of $\pi^0\omega$ and $\eta\omega$ Events

All 1,173,000 5 PED events were then submitted to two independent 6C kinematic fits (see section 3.3) testing the hypotheses that the events were either $\pi^0\omega$ or $\eta\omega$ events with $(\pi^0, \eta) \to \gamma\gamma$ and $\omega \to 3\gamma$. The advantages of fitting directly the $\omega$ decaying to three $\gamma$'s are the following:

- If intermediate states like $\pi^0\eta\gamma$ or $\eta\eta\gamma$ with one single $\gamma$ are fitted, more background from $6\gamma$ events (e.g. $3\pi^0$ or $\pi^0\pi^0\eta$) survive since $E$ and $\vec{p}$ of the single $\gamma$ are only present in 4-momentum conservation but in no additional constraining equation. In addition, many $\pi^0\pi^0\gamma$ events from $\pi^0\omega$ fit equally well the $\pi^0\eta\gamma$ hypothesis thus making an analysis of the $\pi^0\omega$ channel nearly impossible.
- To extract a branching ratio from the observed number of $\omega \to \eta\gamma$ events, one has to normalize on the well known $\omega \to \pi^0\gamma$ decay[3]. This normalization is easy to perform if one fits $\omega \to 3\gamma$ since the $\omega \to \pi^0\gamma$ events are extracted with the same method as the $\omega \to \eta\gamma$ events and both decay modes are present in the same data sample. This is not the case if the hyptheses $\pi^0\pi^0\gamma$, $\pi^0\eta\gamma$ and $\eta\eta\gamma$ are fitted where the systematics and the required cuts may be quite different for $\omega \to \pi^0\gamma$ and $\omega \to \eta\gamma$ events.

[3]It is possible to normalize on the branching ratio $\overline{p}p \to$ *all neutral* as well but the resulting branching ratio for the $\omega \to \eta\gamma$ decay has larger statistical and systematical errors.

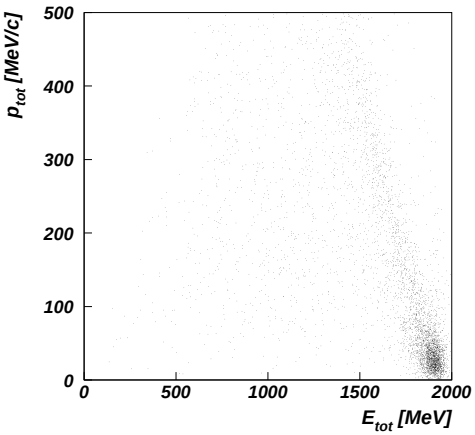


Figure 6: *$E_{tot}$ vs. $p_{tot}$ for a subsample of the 5 PED data sample. The enhancement at 2 GeV and low momentum is due to fully detected events ($E_{tot} = 2m_p$, $p_{tot} = 0$). The band corresponds to events where one $\gamma$ escapes detection. The loss in energy for these events equals the gain in total momentum.*

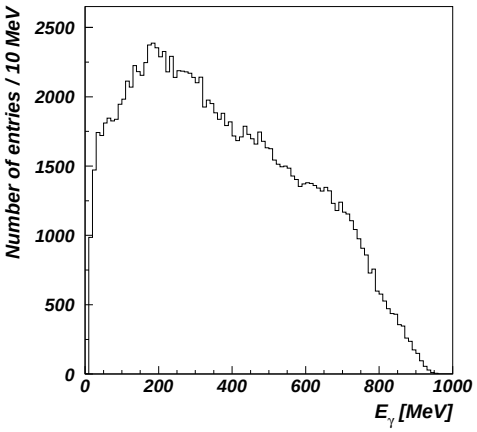


Figure 7: *$E_\gamma$ distribution for a subsample of the 5 PED data sample after the cut on total energy and momentum defined in eqn. 13 has been applied (5 entries/event). Clearly visible is the 10 MeV cut on the energy.*

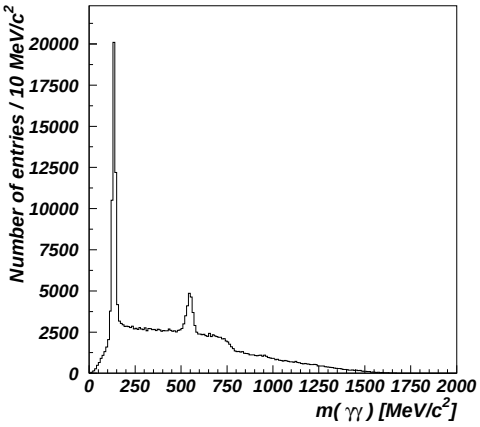


Figure 8: *$m(\gamma\gamma)$ distribution for a subsample of the 5 PED data sample after the cut on total energy and momentum defined in eqn. 13 has been applied (10 entries/event). The two peaks correspond to $\pi^0 \to \gamma\gamma$ and $\eta \to \gamma\gamma$.*

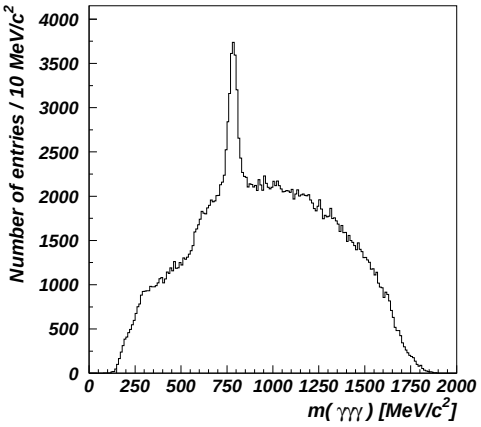


Figure 9: *$m(\gamma\gamma\gamma)$ distribution for a subsample of the 5 PED data sample after the cut on total energy and momentum defined in eqn. 13 has been applied (10 entries/event). The peak corresponds to $\omega \to 3\gamma$.*

- An analysis of the $\omega \to 3\gamma$ Dalitz plot is possible which allows to search for the direct $\omega \to 3\gamma$ decay.

After the two fits, events were selected as potential $\pi^0\omega$ and/or $\eta\omega$ events, if the confidence level (CL) for that hypothesis exceeds 1%. The combination of $\gamma$'s assigned to the $\omega$ and the $\eta$ or $\pi^0$ which yields the best CL has been selected. Note that an event can be present in both data-sets. This ambiguity in the selection criteria is deliberate and done to check the correlation between the two hypotheses. The $CL(\pi^0\omega)$ vs. $CL(\eta\omega)$ is plotted for potential $\pi^0\omega$ and $\eta\omega$ events in figures 10 and 11, respectively. In order to see the weak structures in the center of the plot, the distribution is truncated at 50 events.

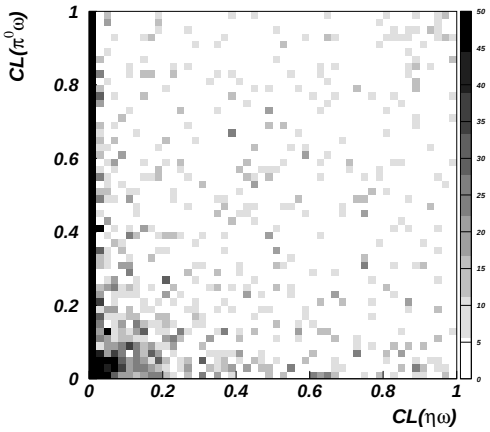


Figure 10: *$CL(\pi^0\omega)$ vs. $CL(\eta\omega)$ for potential $\pi^0\omega$ events. The distribution is truncated at 50 events (maximum bin entry before cut: 7132).*

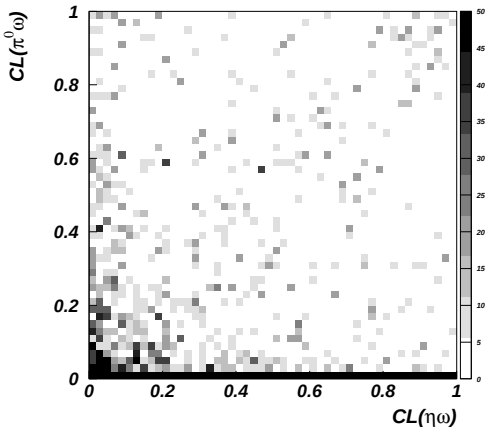


Figure 11: *$CL(\pi^0\omega)$ vs. $CL(\eta\omega)$ for potential $\eta\omega$ events. The distribution is truncated at 50 events (maximum bin entry before cut: 6108).*

Strong bands near the axis are apparent in both figures. These bands originate from events which fit only the selected hypothesis ($\pi^0\omega$ in figure 10 and $\eta\omega$ in figure 11). For these events, obviously no ambiguity between the two hypotheses exists. However, events visible in the center of the plot fit equally well to both hypotheses and an assignment of these events to either of the two event types is not possible. Therefore, in order to separate the two data sets, cuts on confidence levels which only select the narrow bands near the axis have to be introduced, which were defined as

$$\begin{array}{ll} CL(\pi^0\omega) > 10\% \text{ and } CL(\eta\omega) < 1\% & \text{for } \pi^0\omega \text{ events and} \\ CL(\eta\omega) > 10\% \text{ and } CL(\pi^0\omega) < 1\% & \text{for } \eta\omega \text{ events.} \end{array} \tag{14}$$

The 1% anti-cut on the other $\omega$ channel rejects events which could not be assigned to either hypothesis. Since these two cuts exclude each other, an event is present in only one data sample. The numbers of events surviving these cuts are listed in table 3.

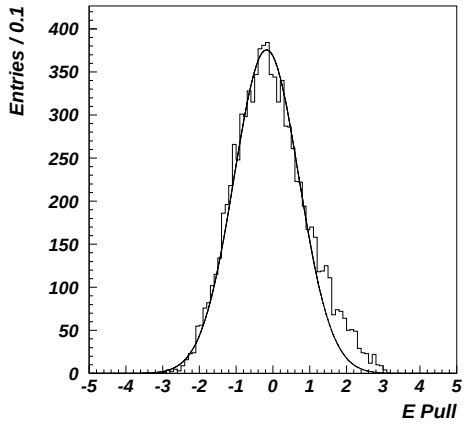


Figure 12: *E pulls for selected $\pi^0\omega$ events for a subsample of the whole data set. The curve shows a fitted Gaussian. The enhancement to positive values is due to energy leakage.*

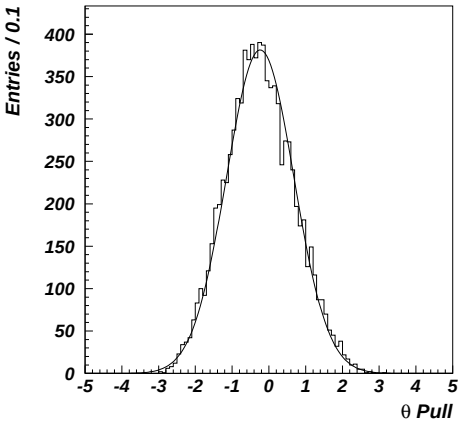


Figure 13: *$\theta$ pulls for selected $\pi^0\omega$ events for a subsample of the whole data set. The curve shows a fitted Gaussian.*

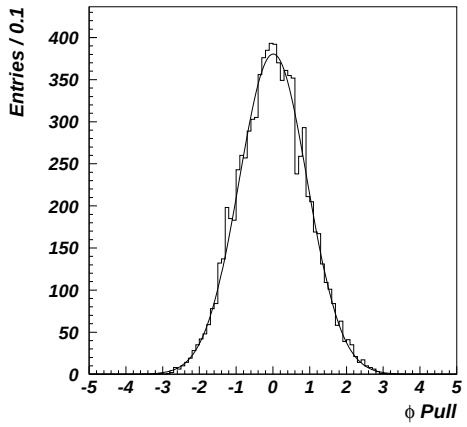


Figure 14: *$\phi$ pulls for selected $\pi^0\omega$ events for a subsample of the whole data set. The curve shows a fitted Gaussian.*

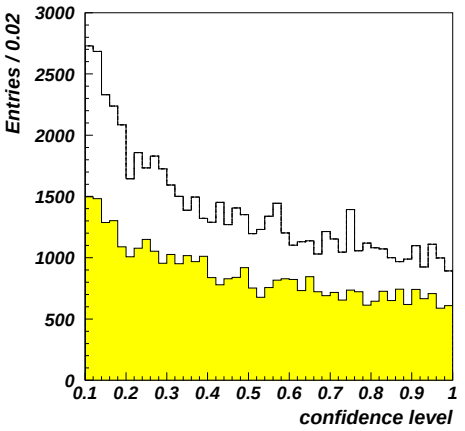


Figure 15: *Confidence level distribution for selected $\pi^0\omega$ events (i.e. with $CL > 0.1$). The dark histogram shows the expected CL distribution from MC $\omega \to \pi^0\gamma$ events.*

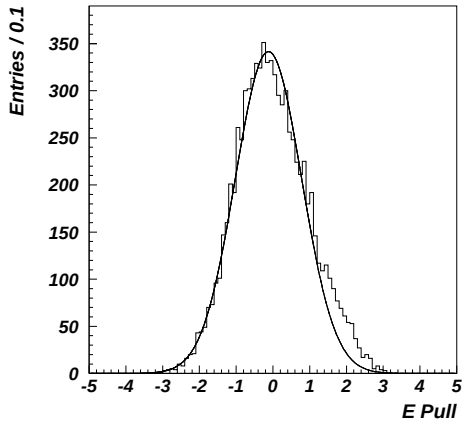


Figure 16: *E pulls for selected $\eta\omega$ events for a subsample of the whole data set. The curve shows a fitted Gaussian. The enhancement to positive values is due to energy leakage.*

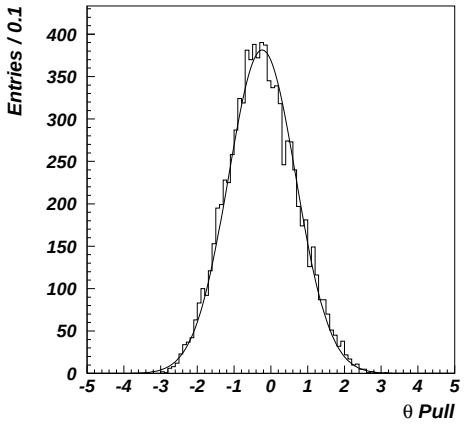


Figure 17: *$\theta$ pulls for selected $\eta\omega$ events for a subsample of the whole data set. The curve shows a fitted Gaussian.*

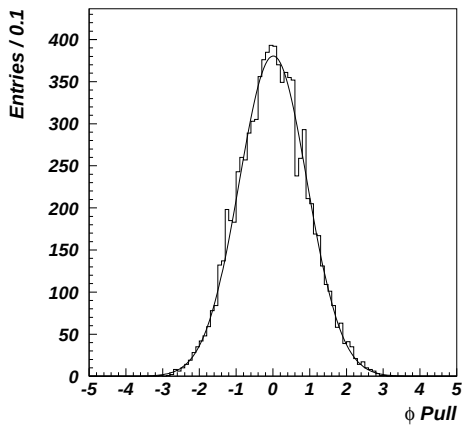


Figure 18: *$\phi$ pulls for selected $\eta\omega$ events for a subsample of the whole data set. The curve shows a fitted Gaussian.*

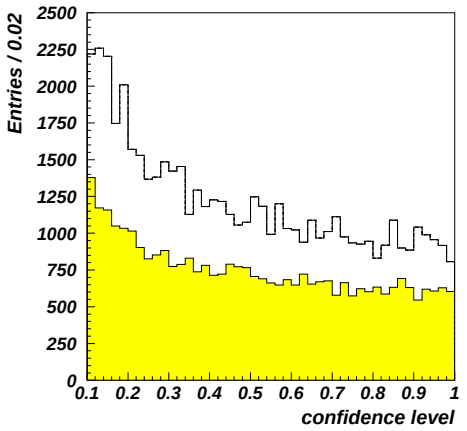


Figure 19: *Confidence level distribution for selected $\eta\omega$ events (i.e. with $CL > 0.1$). The dark histogram shows the expected CL distribution from MC $\omega \to \pi^0\gamma$ events.*

The figures on *p.* 17 and *p.* 18 show fit related histograms for selected $\pi^0\omega$ and $\eta\omega$ events (after the cut defined in eqn. 14 has been applied): the pulls for the three measured variables $E$, $\theta$ and $\phi$ as well as the confidence level distribution for selected $\pi^0\omega$ events on *p.* 17 and the same plots for selected $\eta\omega$ events on *p.* 18. The pull distribution for $E$ (figs. 12 and 16) is not symmetric but shows an enhancement to positive values. This is due to energy leakage in the crystals near the beam pipe. The constraints on 4-momentum conservation increases the energies of the photons hitting these crystals.

The confidence level distributions are shown in figures 15 and 19. The superimposed dark histogram shows the CL for MC $\omega \to \pi^0\gamma$ events. These distributions are not flat but show an enhancement towards low confidence level. One would expect a flat CL distribution at least for generated MC events corresponding to the fit hypothesis, if the errors are correctly estimated. But the situation is more complicated if one fits the $\omega$: the kinematic fit routine assumes an infinitely narrow $\omega$ at its nominal mass of 782 MeV. Thus, after the fit, all events surviving the cuts have $m(3\gamma) = 782$ MeV. But the real $\omega$ events as well as $\omega$'s generated by MC have a Breit-Wigner line-shape with a width of $\Gamma = 8.4$ MeV. Due to this natural width which is not taken into account by the kinematic fit routine, the corresponding pulls are greater than expected just from the experimental resolution alone. The resulting $\chi^2$ is therefore higher, leading to a lower confidence level. The CL distribution for data events are in good agreement with the expected CL distribution expect for low confidence levels, where an enhancement in both channels is visible. This indicates the presence of residual background.

The resulting decay Dalitz plots $\omega \to 3\gamma$ for $\pi^0\omega$ and $\eta\omega$ events are shown in figure 20 and figure 21, respectively. The momenta of the three $\gamma$'s in the $\omega$ rest frame are used to define the Dalitz plot variables

$$X = \frac{T_2 - T_1}{\sqrt{3}Q}, Y = \frac{T_3}{Q} - \frac{1}{3}, \tag{15}$$

where $T_1, T_2, T_3$ are the kinetic energies of the three $\gamma$'s and $Q = T_1 + T_2 + T_3$. Every event is entered 6 times to obtain a symmetric representation. The Dalitz plots show very prominent $\pi^0$ bands near the edge of phase space and weak $\eta$ bands in the center. To show that these structures do not originate from fluctuation of the reconstruction efficiency, the $\omega \to 3\gamma$ Dalitz plots for Monte Carlo $\pi^0\omega, \omega \to 3\gamma$ and $\eta\omega, \omega \to 3\gamma$ events is plotted in figures 22 and 23,

| Hypothesis | Number of events |
|---|---|
| $\pi^0\omega, \omega \to 3\gamma$<br>$CL(\pi^0\omega) > 10\%$ and $CL(\eta\omega) < 1\%$ | 62,853 |
| $\eta\omega, \omega \to 3\gamma$<br>$CL(\eta\omega) > 10\%$ and $CL(\pi^0\omega) < 1\%$ | 54'865 |

Table 3: *Number of surviving events*

respectively. The acceptance is fairly flat in the region of the $\eta$ band, while a slight enhancement at the corners is visible.

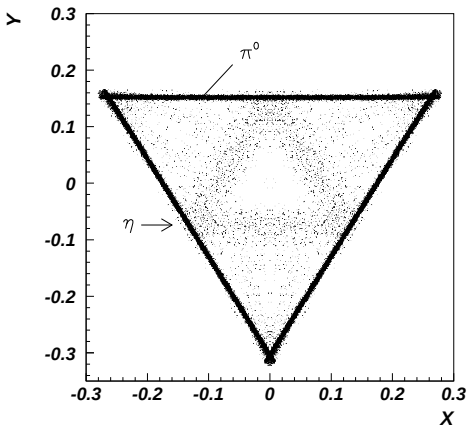


Figure 20: $\omega \to 3\gamma$ *Dalitz plot for selected* $\pi^0\omega$ *events.*

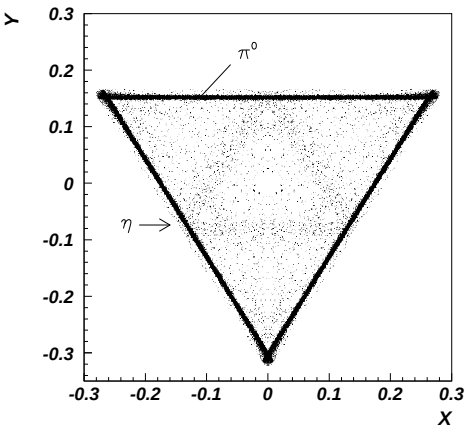


Figure 21: $\omega \to 3\gamma$ *Dalitz plot for selected* $\eta\omega$ *events.*

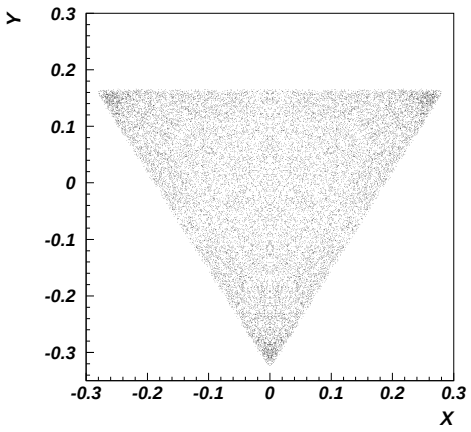


Figure 22: $\omega \to 3\gamma$ *Dalitz plot for Monte Carlo* $\pi^0\omega, \omega \to 3\gamma$ *events (out of 20,000* $\pi^0\omega, \omega \to 3\gamma$ *events).*

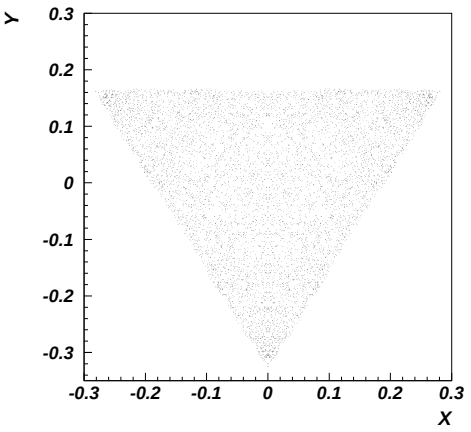


Figure 23: $\omega \to 3\gamma$ *Dalitz plot for Monte Carlo* $\eta\omega, \omega \to 3\gamma$ *events (out of 6,202* $\pi^0\omega, \omega \to 3\gamma$ *events).*

# 5 Monte Carlo Simulations

This chapter describes how background contributions and reconstruction efficiencies are estimated using Monte Carlo (MC) techniques. Two different types of background are discussed: background from final states with 6 $\gamma$'s for which one $\gamma$ escapes detection and background events with 5 $\gamma$'s.

## 5.1 Background Simulation of Events with 6 $\gamma$'s

The main problem in analysing a channel with 5 $\gamma$'s is background from events with final states with 6 $\gamma$'s. If one of the $\gamma$'s lies below detection threshold or is lost because it merged with an other $\gamma$, the total energy and momentum is conserved and the event fakes a perfect 5 $\gamma$ event. These events may in turn fulfill the $\pi^0\omega$ or $\eta\omega$ hypothesis.

The main concern lies in background channels which fake an $\omega \to \eta\gamma$ signal. These channels are $\pi^0\pi^0\eta$ for $\pi^0\omega$ events and $\pi^0\eta\eta$ for $\eta\omega$ events for which one low energy $\gamma$ from a $\pi^0$ decay is lost. Also, since one is interested in the $\omega \to \pi^0\gamma$ decay for normalization, background from $\pi^0\pi^0\pi^0$ has to be kept in mind.

The method to simulate the number of background events passing the analysis and their location in the $\omega \to 3\gamma$ Dalitz plot is based on the Crystal Barrel Monte Carlo software package CBGEANT, which was used to generate events of the types $\pi^0\pi^0\pi^0$, $\pi^0\pi^0\eta$ and $\pi^0\eta\eta$. The Monte Carlo software generates the events according to phase space. However, the data Dalitz plots of 3 pseudoscalar final states show rich resonance structure, which have been previously analysed by the Crystal Barrel Collaboration and reported for instance in ref. [12]. Thus phase space distributed Monte Carlo events do not provide a faithful description.

In the following, the weighting of events according to the real dynamics is described. The generated Monte Carlo events, before reconstruction, are entered in the corresponding Dalitz plots $\pi^0\pi^0\pi^0$, $\pi^0\pi^0\eta$ and $\pi^0\eta\eta$. The bin size is chosen to be the same as for real data events in these final states, i.e. $(0.027\times0.027)$ GeV$^4/c^8$ for $\pi^0\pi^0\pi^0$, $(0.029 \times 0.029)$ GeV$^4/c^8$ and $(0.02 \times 0.02)$ GeV$^4/c^8$ for $\pi^0\eta\eta$.

The weight of each MC event is then given by the number of entries in the corresponding bin of the data Dalitz plots. To directly compare data plots with MC generated plots, one has to normalize the MC data sample to the number of $\overline{p}p$ annihilations in the all neutral data sample. The derivation of the normalization constant $f$ can be found in appendix B. The error on a bin in a weighted histogram is derived in appendix C.

These weighted events are reconstructed in the following as $\pi^0\omega$ and $\eta\omega$ events using the same method as for real data (see section 4). Note that the reconstruction is based on photons smeared by the experimental resolution and hence includes also the combinatorics in the assignement of photons to $\pi^0$'s and/or $\eta$'s.

First, background from $\pi^0\pi^0\pi^0$ is discussed. Figure 24 shows the $3\pi^0$ Dalitz plot of events which survive the criteria of being $\pi^0\omega$ as well as their location in the $\omega \to 3\gamma$ Dalitz plot. Note that in the case of $3\pi^0$, one lost $\gamma$ leads to a detected $\pi^0\pi^0\gamma$ event which fakes $\pi^0\omega, \omega \to \pi^0\gamma$. This decay $\pi^0$ is observed as

| | $\pi^0\omega$ | $\eta\omega$ | on page |
|---|---|---|---|
| $\pi^0\pi^0\pi^0$ | 5,168 | 959 | 24 |
| $\pi^0\pi^0\eta$ | 1,263 | 1,476 | 25 |
| $\pi^0\eta\eta$ | 9 | 265 | 26 |

Table 4: *Summary of surviving background events in both channels. The last column gives the page on which the histograms for this background channel can be found.*

strong bands in the $\omega \to 3\gamma$ Dalitz plot. The total number of $3\pi^0$ events in $\pi^0\omega$ is found to be 5,168. Background from $3\pi^0$ is less serious in the $\eta\omega$ channel since the $\eta$ is only reconstructed due to $\gamma\gamma$ combinations forming accidentally an $\eta$. The $\omega \to 3\gamma$ Dalitz plot for reconstructed $3\pi^0$ events in the $\eta\omega$ channel is shown in figure 25 right. Also in $\eta\omega$, events accumulate mainly in the $\pi^0$ bands of the $\omega$ decay Dalitz plot. The total background contamination is 959. It is stressed that only a few events are found in the $\eta$ region of the $\omega$ decay Dalitz plot since the probability for finding two $\eta$'s in $3\pi^0$ is rather low.

The next background channel which is studied is $\overline{p}p \to \pi^0\pi^0\eta$. The $\pi^0\pi^0\eta$ Dalitz plot for events which fake a $\pi^0\omega$ event is shown in figure 26 left. Note that the main contribution stems from $\overline{p}p \to a_2^0, a_2^0 \to \pi^0\eta$ which is responsible for the enhancement at low $\pi^0\eta$ invariant masses. The same events in the $\omega \to 3\gamma$ Dalitz plot (figure 26 right) do not show strong structures except that the region in the center of the plot has no events at all. This is due to the limit of phase space for surviving $\overline{p}p \to \pi^0\pi^0\eta$ events. However, a faint band where the $\eta$ is expected is visible and stems from the decay $a_2 \to \pi^0\eta$, where one photon from the $\pi^0$ decay escapes detection. From a total of 1,273 background events from $\pi^0\pi^0\eta$ in $\pi^0\omega$, about 300 events are found in the $\eta$ region. This is the dominant background for the measurement of $\omega \to \eta\gamma$ in $\pi^0\omega$ (see section 6.2). Background from $\pi^0\pi^0\eta$ is also important in the channel $\eta\omega$. The events surviving the criteria of being $\eta\omega$ are shown in the $\pi^0\pi^0\eta$ Dalitz plot (figure 27 left) and in the $\omega$ decay Dalitz plot (figure 27 right). The total number of background events is 1,476. Unlike in the case of $\pi^0\omega$, these background events accumulate in the $\pi^0\pi^0\eta$ Dalitz plot along the diagonal corresponding to the recoiling momentum of an $\eta$ from $\overline{p}p \to \eta\omega$. One photon of the decaying $\pi^0$'s is lost and the events fakes an $\omega \to \pi^0\gamma$ decay visible as strong $\pi^0$ bands in the $\omega$ decay Dalitz plot. Due to wrong $\gamma\gamma$ combinations, the (real) $\eta$ shows also up as $\eta$ bands in figure 27 right.

A negligible number of 9 background events from $\pi^0\eta\eta$ is found in the $\pi^0\omega$ channel (figure 26). The reason for this small feedthrough probability lies in the fact that only the $\pi^0$ can emit a photon below the detection threshold and hence the reconstructed $\pi^0$ from $\pi^0\omega$ is due to accidentally $\gamma\gamma$ combinations being fitted to a $\pi^0$. The same background, $\pi^0\eta\eta$, is more prominent in the $\eta\omega$ channel and leads to 205 events in the $\omega$ decay Dalitz plot. This is the dominant background

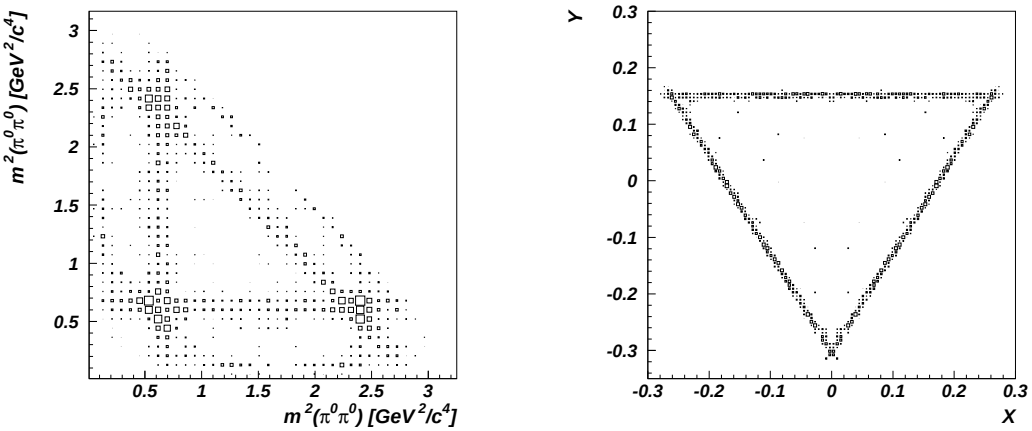


Figure 24: *Background contribution from $\pi^0\pi^0\pi^0$ in $\pi^0\omega$. Left histogram: Position of background events in the $\pi^0\pi^0\pi^0$ Dalitz plot. Right histogram: Position of background events in the $\omega \to 3\gamma$ Dalitz plot. The total number of background events is 5168.*

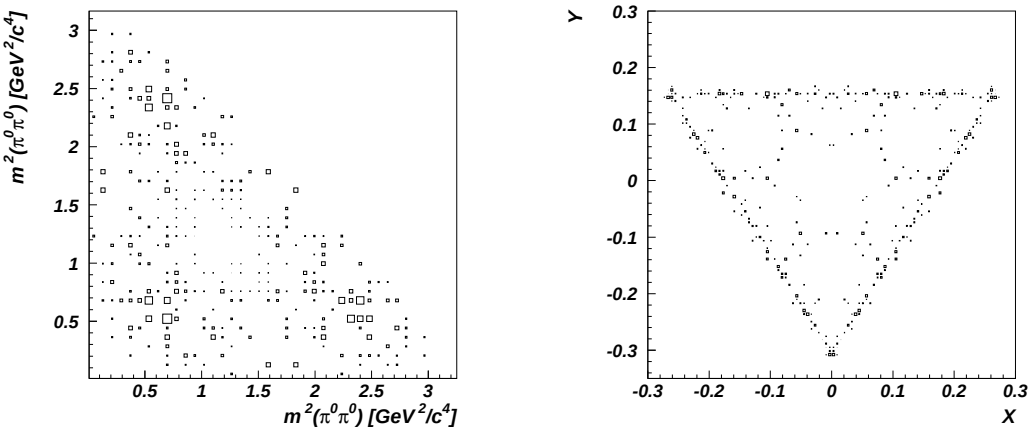


Figure 25: *Background contribution from $\pi^0\pi^0\pi^0$ in $\eta\omega$. Left histogram: Position of background events in the $\pi^0\pi^0\pi^0$ Dalitz plot. Right histogram: Position of background events in the $\omega \to 3\gamma$ Dalitz plot. The total number of background events is 959.*

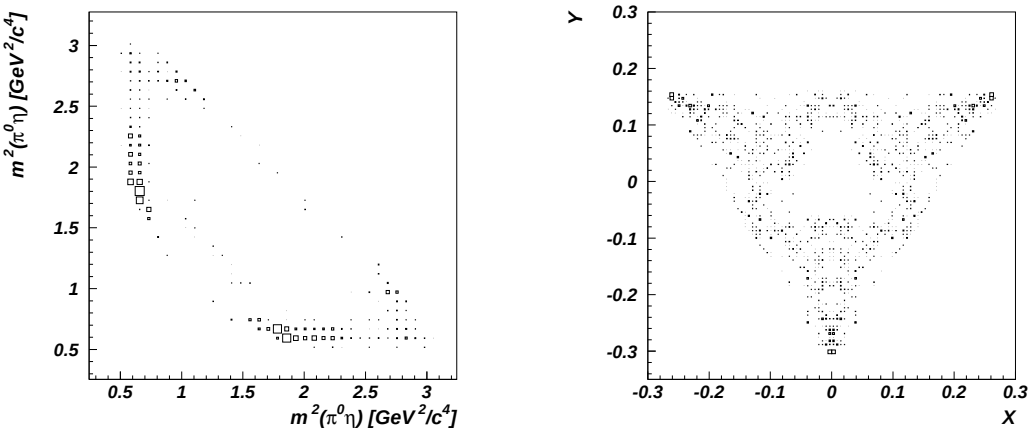


Figure 26: *Background contribution from $\pi^0\pi^0\eta$ in $\pi^0\omega$. Left histogram: Position of background events in the $\pi^0\pi^0\eta$ Dalitz plot. Right histogram: Position of background events in the $\omega \to 3\gamma$ Dalitz plot. The total number of background events is 1263.*

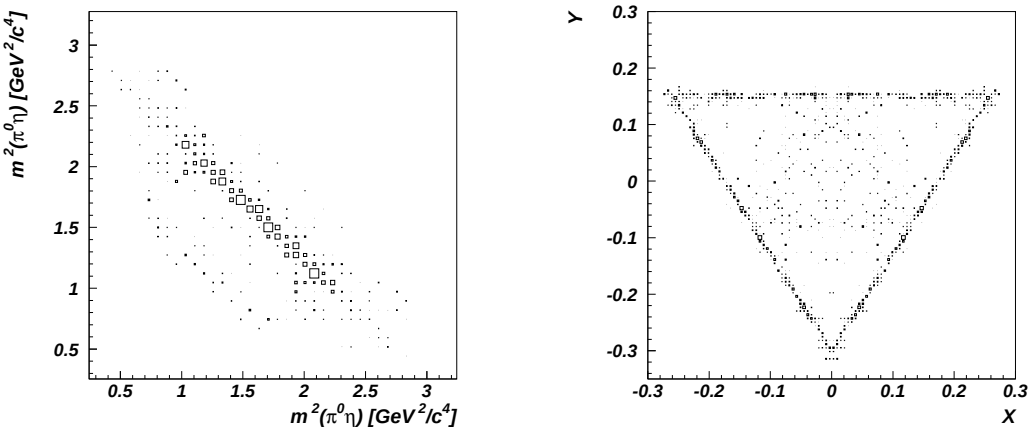


Figure 27: *Background contribution from $\pi^0\pi^0\eta$ in $\eta\omega$. Left histogram: Position of background events in the $\pi^0\pi^0\eta$ Dalitz plot. Right histogram: Position of background events in the $\omega \to 3\gamma$ Dalitz plot. The total number of background events is 1476.*

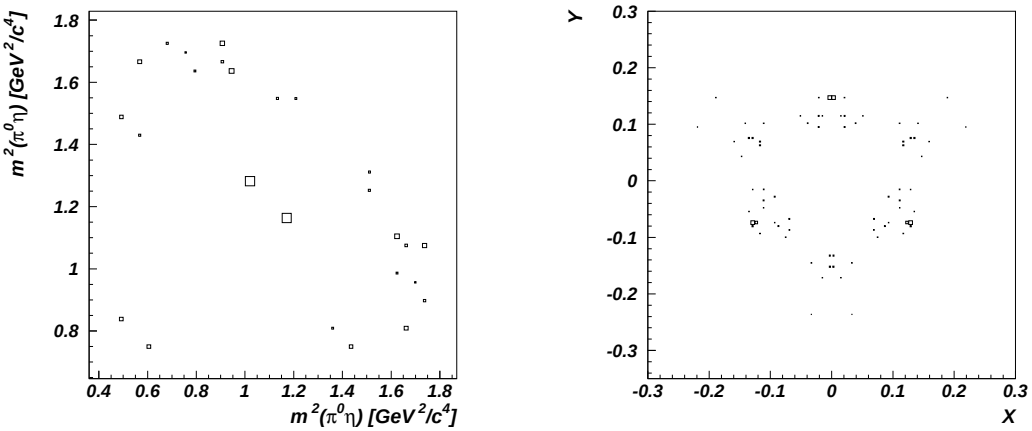


Figure 28: *Background contribution from $\pi^0\eta\eta$ in $\pi^0\omega$. Left histogram: Position of background events in the $\pi^0\eta\eta$ Dalitz plot. Right histogram: Position of background events in the $\omega \to 3\gamma$ Dalitz plot. The total number of background events is 9.*

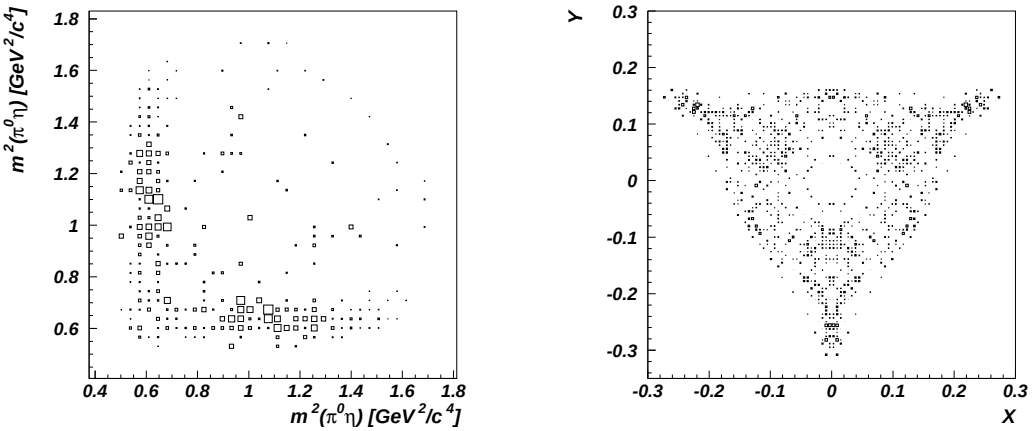


Figure 29: *Background contribution from $\pi^0\eta\eta$ in $\eta\omega$. Left histogram: Position of background events in the $\pi^0\eta\eta$ Dalitz plot. Right histogram: Position of background events in the $\omega \to 3\gamma$ Dalitz plot. The total number of background events is 265.*

channel which has to be considered in the analysis of $\eta\omega$ (see section 6.1).

To summarize, background from the 3 pseudoscalar final states $\pi^0\pi^0\pi^0$, $\pi^0\pi^0\eta$ and $\pi^0\eta\eta$ lead to important contributions in $\omega$ decay Dalitz plots from the reactions $\overline{p}p \to \pi^0\omega$ and $\overline{p}p \to \eta\omega$. The number of background events from each channel in $\pi^0\omega$ and $\eta\omega$ is listed in table 4.

It is noted that some of these numbers will be reduced further when the branching ratio $\omega \to \eta\gamma$ is measured.

## 5.2 Background Simulation of Events with 5 $\gamma$'s

The Monte Carlo background simulation of $5\gamma$ events is much easier to handle than the one for $6\gamma$ events. Events with $5\gamma$ originate from $\overline{p}p \to X\omega$, where $\omega \to \pi^0\gamma$ and $X = (\pi^0, \eta)$. In these two-body reactions, the particles have fixed momenta and no dynamics of intermediate resonances have to be considered. However, the $\omega \to \pi^0\gamma$ angular distribution must be taken into account. The angular distribution is isotropic in CBGEANT, whereas the expected angular distribution is of the form [14] [15]

$$\frac{dN}{d\cos\theta} \propto 1 + b\cos^2\theta, \tag{16}$$

considering both $S$- and $P$-wave annihilation. The parameter $b$ was measured for $\overline{p}p$ annihilation at rest into $\pi^0\omega$ in ref. [15]. They find $b \simeq 0.82$ which is used in the present work for all radiative $\omega$ decays.

The non isotropic $\omega$-decay distribution is taken into account in the following way: to simulate $\eta\omega, \omega \to \pi^0\gamma$ events, phase space distributed events of type $\pi^0\eta\gamma$ are generated. The generated kinematic variables of the three particles are read from the KINE bank and used to weight every single event. To obtain events of type $\omega \to \pi^0\gamma$, the invariant mass $m(\pi^0\gamma)$ of each event is weighted with a Breit-Wigner function of the form

$$BW = \frac{1}{m - m_0 - i\Gamma_0/2}, \tag{17}$$

where $m = m(\pi^0\gamma)$ and $m_0, \Gamma_0$ are the resonance parameters of the $\omega$, $m_0 = 781.9$ MeV, $\Gamma_0 = 8.43$ MeV [11]. In addition, the decay angle $\omega \to \pi^0\gamma$ in the $\omega$ rest frame can be calculated using

$$\cos\theta^* = \frac{1}{\beta}\left(\frac{E_\gamma}{\gamma E^*_\gamma} - 1\right), \tag{18}$$

where $\beta$ and $\gamma$ are the speed and $\gamma$-factor of the $\omega$ and

$$E^*_\gamma = \frac{m^2(\pi^0\gamma) - m^2_{\pi^0}}{2m(\pi^0\gamma)} \tag{19}$$

is the energy of the $\gamma$ in the $\omega$ rest frame. The decay angle is then weighted according to eqn. 16. After weighting the events, the whole MC data sample has to be scaled to the expected number of events of the type concerned.

To calculate the number of expected events, the following branching ratios are used [11] [13]:

$$\begin{aligned} BR(\overline{p}p \to \pi^0\omega) &= (5.73 \pm 0.47) \times 10^{-3}, \\ BR(\overline{p}p \to \eta\omega) &= (1.51 \pm 0.12) \times 10^{-2}, \\ BR(\eta \to \gamma\gamma) &= (38.8 \pm 0.5)\%, \\ BR(\omega \to \pi^0\gamma) &= (8.5 \pm 0.5)\%. \end{aligned} \tag{20}$$

| Event type | $N^{exp}$ |
|---|---|
| $\pi^0\omega, \omega \to \pi^0\gamma, \to 5\gamma$ | $193,000 \pm 24,500$ |
| $\eta\omega, \omega \to \pi^0\gamma, \to 5\gamma$ | $197,400 \pm 24,700$ |

Table 5: *Summary of 5$\gamma$ events. $N^{exp}$: Number of expected events in the all neutral data sample used in this work.*

The method to calculate the expected number of events can be found in appendix B.

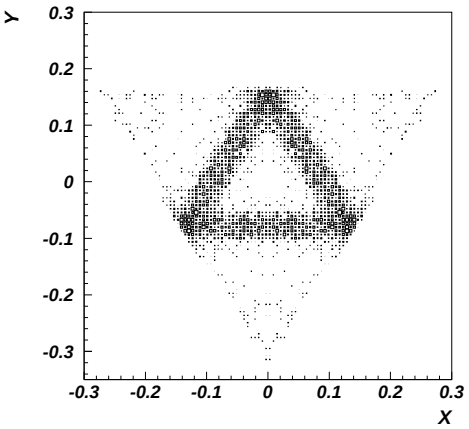


Figure 30: *Background contribution from $\eta\omega(\omega \to \pi^0\gamma)$ in the $\pi^0\omega$ channel. The total number of background events is 130.*

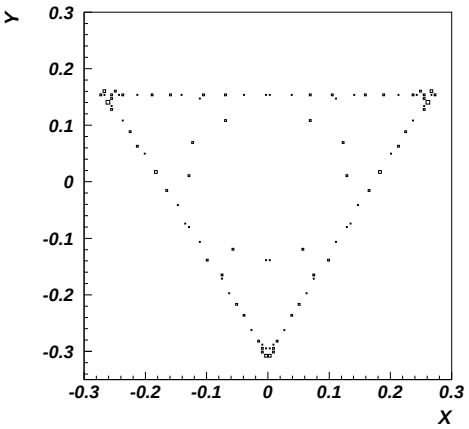


Figure 31: *Background contribution from $\pi^0\omega(\omega \to \pi^0\gamma)$ in the $\eta\omega$ channel. The total number of background events is 76.*

The resulting $\omega \to 3\gamma$ Dalitz plots for background events from other $\omega$ channels is shown in figures 30 and 31.

Background from $\eta\omega$ in the $\pi^0\omega$ clearly fakes an $\omega \to \eta\gamma$ signal. Thus for a measurement of the $\omega \to \eta\gamma$ branching ratio in $\pi^0\omega$, background from $\eta\omega$ has to be subtracted. The total number of background events is 130.

The background from $\pi^0\omega$ in $\eta\omega$ has almost every events in the $\omega \to \pi^0\gamma$ band. The total number of background events is 76.

## 5.3 Reconstruction Efficiencies of $\pi^0\omega$ and $\eta\omega$

The calculation of reconstruction efficiencies is straightforward: one generates MC events with the required intermediate states, applies the same fits and cuts as for data events and counts the number of surviving events. The reconstruction efficiency is then given by

$$\varepsilon = \frac{N^{surviving}}{N^{generated}}. \tag{21}$$

Usually, the efficiency does not depend on $\cos\theta^*$. However, if one applies cuts on the angular distribution or on invariant masses, the acceptance depends on the decay angle. In that case, the method presented in section 5.2 is used to generate MC events with a more appropriate angular distribution.

# 6 Analysis

## 6.1 The $\eta\omega$ Channel

In this section, an analysis of the $\eta\omega$ channel is described. The aim was to measure the $\omega \to \eta\gamma$ branching ratio. Since the relative contribution from $\eta\rho, \rho \to \eta\gamma$ is suppressed due to the low branching ratio for the $\rho$ production [11] [13] [16]

$$\frac{BR(\overline{p}p \to \eta\omega)}{BR(\overline{p}p \to \eta\rho)} \cdot \frac{BR(\omega \to \eta\gamma)}{BR(\rho \to \eta\gamma)} \simeq 5.8, \tag{22}$$

and the broad nature of the $\rho$, the coherent background from $\rho \to \eta\gamma$ is very small. This is not the case for the $\pi^0\omega$ channel, where the ratio in eqn. 22 is $\simeq 0.73$ (see section 6.2). A detailed analysis of $\pi^0\omega$ and $\eta\omega$ taking into account the $\rho$ contribution is the subject of section 6.4.

Figure 32 and 33 show a one-dimensional projection of the $\omega \to 3\gamma$ Dalitz plot (fig. 21) for the $\eta\omega$ channel.

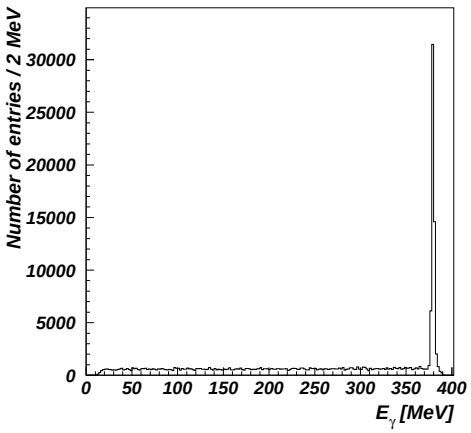


Figure 32: *$E_\gamma$ in the $\omega$ rest frame (3 entries/event).*

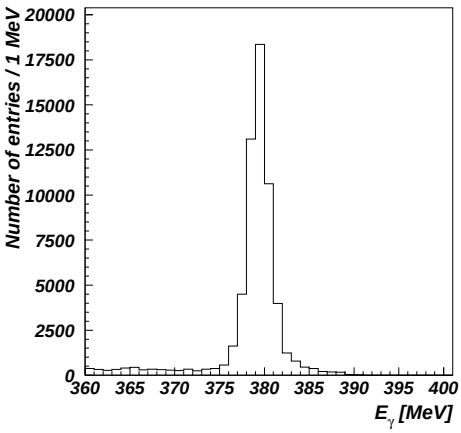


Figure 33: *Same as in fig. 32 but with enlarged horizontal scale. The peak is due to $\omega \to \pi^0\gamma$ .*

A clear peak around 380 MeV is visible, coming from radiative $\gamma$'s from $\omega \to \pi^0\gamma$ ($E_\gamma = 379.3$ MeV for $m_\omega = 782$ MeV/$c^2$). The broad band from 10 to 390 MeV is due to reflection from $\omega \to \pi^0\gamma$ events. Since $J(\pi^0) = 0$, the decay process $\pi^0 \to \gamma\gamma$ is isotropic, and hence, the $\pi^0$ bands are flat. This type of 'background' events are called 'combinatorial background' in the present work although they do *not* originate from real background events but from reflection in the Dalitz plot.

To count the number of $\omega \to \pi^0\gamma$ events, simulated background from $\pi^0\pi^0\pi^0$ and $\pi^0\pi^0\eta$ (as described in section 5.1) is subtracted. The number of background events is:

$$\begin{array}{lcr} \pi^0\pi^0\pi^0 & : & 959 \\ \pi^0\pi^0\eta & : & 1,476 \\ \pi^0\eta\eta & : & 265 \end{array} \tag{23}$$

After subtracting the background and assuming a flat combinatorial background under the $\pi^0$ peak, the number of events in the peak is:

$$N_{\omega\to\pi^0\gamma} = 50430 \pm 239. \tag{24}$$

The reconstruction efficiency for these events is simulated with Monte Carlo events of the type $\overline{p}p \to \eta\omega(\omega \to \pi^0\gamma) \to 5\gamma$. Out of 77,487 generated MC events, $N_{\omega\to\pi^0\gamma} = 16,507 \pm 131$ survive the cuts. The reconstruction efficiency for $\omega \to \pi^0\gamma$ is therefore

$$\varepsilon_{\omega\to\pi^0\gamma} = (21.3 \pm 0.2)\%, \tag{25}$$

where the error is statistical only. Eqn. 24 and 25 will be used to normalize the number of observed $\omega \to \eta\gamma$ events to the known branching ratio for $\omega \to \pi^0\gamma$.

An $\eta$ signal, clearly visible in the Dalitz plot (figure 21), is not seen in figure 32 due to the broad combinatorial background from $\omega \to \pi^0\gamma$. To suppress events with $\omega \to \pi^0\gamma$, one has to reject every event that has at least one $\gamma$ in the $\pi^0$ peak. Hence events were rejected whenever

$$|E_\gamma \text{ [MeV]} - 379| < 15 \tag{26}$$

for at least one $\gamma$.

However, if one plots for the remaining (potential $\omega \to \eta\gamma$) events the invariant mass $m^2(\gamma\gamma)$ for which one $\gamma$ stems from $\omega \to 3\gamma$ and the other originates from the recoiling $\eta$, a $\pi^0$ peak is observed (see figure 34). The events in the $\pi^0$ peak are due to $\eta\omega(\omega \to \pi^0\gamma)$ events for which the kinematic fit assigned wrong $\eta$ and $\omega$ combinations[4], and to a lesser extent, due to background events from $\pi^0\pi^0\eta$. A fit to the $\pi^0$ peak using a Gaussian and a second order polynomial gives for the Gaussian: $m = (135.6 \pm 0.27)$ MeV/$c^2$ and $\sigma = (8.4 \pm 0.28)$ MeV/$c^2$. An additional $3\sigma$ cut on these $\pi^0$'s is therefore introduced, rejecting events for which

$$|m(\gamma\gamma) \text{ [MeV/}c^2\text{]} - 135| < 25 \tag{27}$$

for any $\gamma\gamma$ combination for which one $\gamma$ originates from $\omega \to 3\gamma$ and the other $\gamma$ is assigned to the $\eta$. The resulting histogram, figure 35, shows a clear $\eta$ peak around 200 MeV corresponding to $\omega \to \eta\gamma$ ($E_\gamma = 199.7$ MeV).

Next, background from $5\gamma$ and $6\gamma$ events has to be subtracted. Only final states which have at least one $\eta$ have been considered as possible background, since only these events can fake an $\omega \to \eta\gamma$ signal (see subsections 5.1 and 5.2 for all possible background histograms). The number of residual background after the two $\pi^0$ cuts (as defined in eqn. 26 and 27) are:

[4]One $\gamma\gamma$ combination was wrongly assigned to an $\eta$ recoiling against the $\omega$. Thus the 'real' $\eta$ fakes an $\omega \to \eta\gamma$ event.

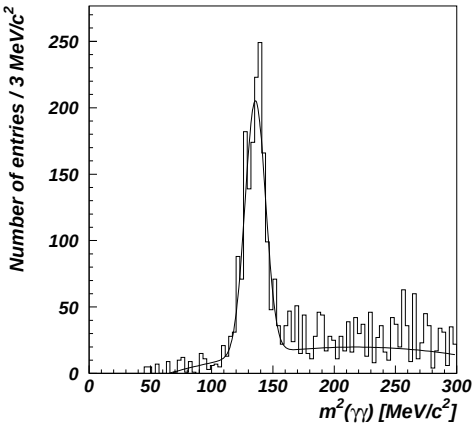


Figure 34: $m^2(\gamma\gamma)$ *distribution for* $\gamma\gamma$ *combination where one* $\gamma$ *is from* $\omega \to 3\gamma$ *and one is from the recoiling* $\eta$*. A clear* $\pi^0$ *peak is observed. The fit is a Gaussian and a 2nd order polynomial.*

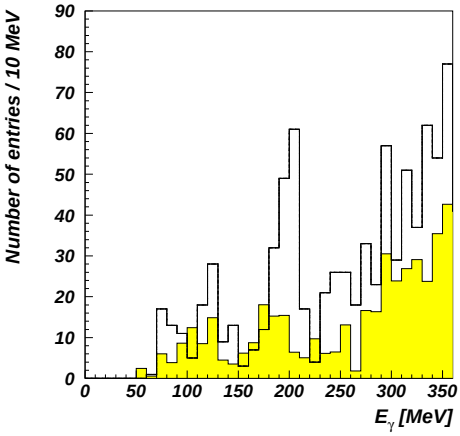


Figure 35: $E_\gamma$ *distribution for events which survive the* $\pi^0$ *cut described in the text. A clear* $\eta$ *peak is visible around 200 MeV, due to* $\omega \to \eta\gamma$ *. The hatched histogram shows the background contribution from* $\pi^0\eta\eta$*.*

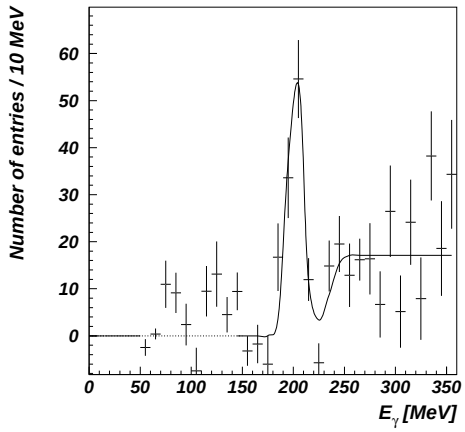


Figure 36: *Same as in figure 35 but after background subtraction. The fit is described in the text.*

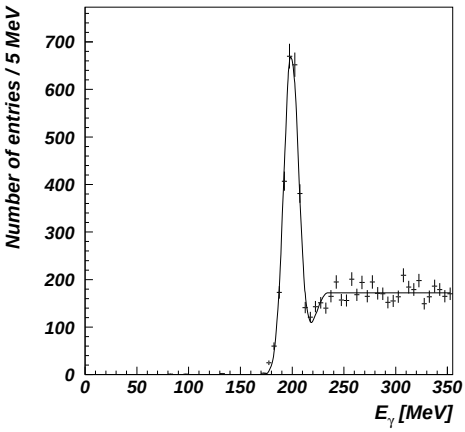


Figure 37: $E_\gamma$ *distribution in the* $\omega$ *rest frame for* $\eta\omega, \omega \to \eta\gamma$ *MC events. The same cuts as for data events have been applied.*

$$\begin{array}{lcr} \pi^0\pi^0\pi^0 & : & 0 \\ \pi^0\pi^0\eta & : & 2 \\ \pi^0\eta\eta & : & 146 \\ \eta\omega(\omega \to \pi^0\gamma) & : & 0 \end{array} \tag{28}$$

Background from $\pi^0\eta\eta$ is therefore dominant. The background from $\eta\omega, \omega \to \pi^0\gamma$ vanishes completely after the introduction of the $\pi^0$ cut on 'false' $\gamma\gamma$ combination (eqn. 27). The feedthrough from $\pi^0\pi^0\eta$ with 2 events is negligible. The simulated feedthrough from $\pi^0\eta\eta$ is shown in figure 35 by the hatched histogram. The background contribution below 150 MeV is underestimated, since no events are expected below that value. This indicates the presence of a systematical error in the background normalization. To estimate this error, the background is subtracted (figure 36) and the region from 50 to 150 MeV is fitted to a constant $A$. The fit yields:

$$A = 1.2 \pm 0.8. \tag{29}$$

This is therefore the systematical error on a bin in the background histogramm.

From figure 35, the number of $\eta$ events can directly be counted by simply integrating the data and the background histograms. The following numbers of events were found for the peak (5 bins from 170 MeV to 220 MeV):

$$\begin{array}{lrcrcr} \text{Data } (\eta\omega): & 171 & \pm & 13 & & \\ \text{Background } (\pi^0\eta\eta): & 60 & \pm & 9 & \pm & 6 \\ \hline \text{Total:} & 111 & \pm & 16 & \pm & 6 \end{array} \tag{30}$$

The first error is statistical, the second systematical. For further calculations, the two errors are combined quadratically:

$$N_{\omega\to\eta\gamma} = 111 \pm 17. \tag{31}$$

A more sophisticated method subtracts the background from the data histogram and fits the resulting histogram in order to obtain the number of events in the $\eta$ peak. The number of events per bin after background subtraction is given by

$$n = n_{data} - n_{BG}, \tag{32}$$

where $n_{data}$ is the number of entries per bin in the data histogram and $n_{BG}$ is the number of entries per bin in the background histogram. The resulting histogram is shown in figure 36.

The parametrization of the fit used to determine the number of $\omega \to \eta\gamma$ events in the background subtracted histogram is given by the shape of the expected energy spectrum from Monte Carlo $\omega \to \eta\gamma$ events (figure 37). The general features of the Monte Carlo distribution are:

1. No events are expected below 170 MeV.

2. The combinatorial background above 250 MeV up to 350 MeV is completely flat.

3. The combinatorial background decreases below 240 MeV. The downward slope was described by half of a Gaussian with $\sigma_{BG} = 1/\cos 60^\circ \cdot \sigma_{peak}$, where $60^\circ$ is the angle between the $\eta$ bands in the $\omega \to 3\gamma$ Dalitz plot.

Note that the slope is determined by the cut introduced in eqn. 26. This cut removes the triangular accumulation of events from $\omega \to \pi^0\gamma$ and affects the corners of the $\omega \to \eta\gamma$ triangle (see Dalitz plot, figure 21). The $\eta$ peak itself is parametrized with a Gaussian. In the fit, the height of the combinatorial background, the begin of the slope of the combinatorial background as well as the three parameters for the Gaussian were treated as free parameters.

The histogram in figure 36 was fitted from 140 to 350 MeV. The dotted line below 140 MeV indicates the baseline. The fit finds the following parameters for the $\eta$ peak:

$$\begin{aligned} E &= (201.8 \pm 1.4) \text{ MeV} \\ \sigma &= (7.15 \pm 1.12) \text{ MeV} \\ A &= (58.9 \pm 9.17) \text{ events/bin.} \end{aligned} \tag{33}$$

The integration of the Gaussian yields the number of observed $\omega \to \eta\gamma$ events,

$$N_{\omega\to\eta\gamma} = 105.7 \pm 23.2. \tag{34}$$

This value is completely consistent with the $111 \pm 17$ events obtained with the bin integrating method.

To determine the reconstruction efficiency for this reaction, the Monte Carlo histogram in figure 37 is fitted. Out of 16,544 generated $\overline{p}p \to \eta\omega(\omega \to \eta\gamma) \to 5\gamma$ MC events, the fit finds $E = (199.09 \pm 0.17)$ MeV, $\sigma = (7.18 \pm 0.16)$ MeV, $A = (670.07 \pm 18.03)$ events/bin. The peak position and width for data and MC events are in perfect agreement, showing that the data are well understood. The number of events in the MC $\eta$ peak is $N_{\omega\to\eta\gamma} = 2405.55 \pm 83.39$. The reconstruction efficiency therefore is

$$\varepsilon_{\omega\to\eta\gamma} = (14.54 \pm 0.54)\%. \tag{35}$$

Since the bin integration method has a slightly smaller error, the value obtained with this method is used for further calculations. The ratio of the two branching ratios $\omega \to \eta\gamma$ and $\omega \to \pi^0\gamma$ is

$$\frac{BR(\omega \to \eta\gamma)}{BR(\omega \to \pi^0\gamma)} = \frac{N_{\omega\to\eta\gamma}}{N_{\omega\to\pi^0\gamma}} \cdot \frac{\varepsilon_{\omega\to\pi^0\gamma}}{\varepsilon_{\omega\to\eta\gamma}} \cdot \frac{BR(\pi^0 \to 2\gamma)}{BR(\eta \to 2\gamma)} = (8.29 \pm 1.31) \times 10^{-3}, \tag{36}$$

from which, after normalizing on the well known branching ratio $BR(\omega \to \pi^0\gamma) = (8.5 \pm 0.5)\%$ [11], it follows

$$BR(\omega \to \eta\gamma) = (7.05 \pm 1.19) \times 10^{-4}. \quad (37)$$

The error is dominated by the error on the number of observed $\omega \to \eta\gamma$ events. The systematical errors on the reconstruction efficiencies of $\omega \to \eta\gamma$ and $\omega \to \pi^0\gamma$ events cancel in good approximation.

The $\omega \to \eta\gamma$ branching ratio has previously been measured only in ref. [5] in a 'model independent' way[5]. They used high energy $\pi^- p \to \omega\, n$ charge-exchange as a source of $\omega$ mesons. They have chosen high momentum transfers $|t|$ in order to suppress $\pi$ exchange and therefore $\rho$ production. However, no estimate of the remaining contamination of coherent background from $\pi^- p \to \rho\, n$ is made. They obtain $BR(\omega \to \eta\gamma) = (8.3 \pm 2.1) \times 10^{-4}$, which is in good agreement with the value measured in this section.

[5]This means that for the determination of the branching ratio no assumption about the behaviour of the $\rho - \omega$ mixing was made.

## 6.2 The $\pi^0\omega$ Channel

In the annihilation channel $\overline{p}p \to \pi^0\omega$ a branching ratio for $\omega \to \eta\gamma$ cannot be measured directly since the production of $\rho$ in $\overline{p}p \to \pi^0\rho$ is much stronger than $\omega$ in $\overline{p}p \to \pi^0\omega$ [11] [13] [16]:

$$\frac{BR(\overline{p}p \to \pi^0\omega)}{BR(\overline{p}p \to \pi^0\rho)} \cdot \frac{BR(\omega \to \eta\gamma)}{BR(\rho \to \eta\gamma)} \simeq 0.73. \tag{38}$$

The coherent contribution from $\rho$ can therefore not be neglected.

However, to gain information about the $\rho - \omega$ mixing, it is very useful to have the number of observed events $(\rho - \omega) \to \eta\gamma$ in the $\pi^0(\rho - \omega)$ channel. The theory of the mixing and a coupled analysis of the two channels $\pi^0(\rho - \omega)$ and $\eta(\rho - \omega)$ are the subject of section 6.4. To simplify matters, the mixed $(\rho - \omega)$ state is called $\omega$ here.

Another problem in analysing the $\pi^0\omega$ channel is intense background from $\pi^0\pi^0\eta$, mainly $\overline{p}p \to \pi^0 a_2, a_2 \to \pi^0\eta$, and from $\eta\omega(\omega \to \pi^0\gamma)$. Thus one heavily relies on Monte Carlo simulation to extract the number of $\omega \to \eta\gamma$ events. Due to this problem, the errors on the extracted values are higher than for $\eta\omega$ events.

The analysis presented here follows the determination of the $\omega \to \eta\gamma$ branching ratio of section 6.1, where the general features of $\omega \to 3\gamma$ events and the data treatment are discussed in details.

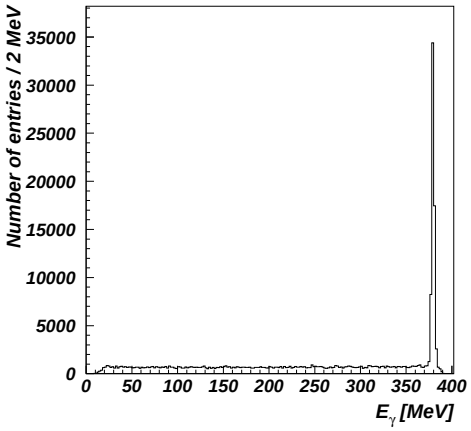


Figure 38: *$E_\gamma$ distribution in the $\omega$ rest frame (3 entries/event).*

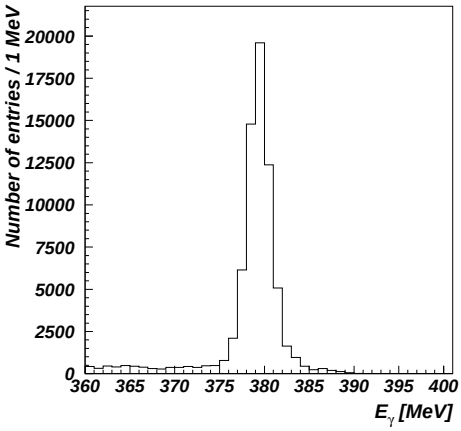


Figure 39: *Same as in fig. 38 but with enlarged horizontal scale. The peak is due to $\omega \to \pi^0\gamma$.*

Figure 39 shows the $\omega \to \pi^0\gamma$ peak for $\pi^0\omega$ events. To count the number of $\omega \to \pi^0\gamma$ events, background from $6\gamma$ events has to be simulated. The number of surviving background events is:

$$\begin{array}{lcr} \pi^0\pi^0\pi^0 & : & 5,168 \\ \pi^0\pi^0\eta & : & 1,263 \\ \pi^0\eta\eta & : & 9 \end{array} \tag{39}$$

After subtraction, and assuming a flat combinatorial background, the number of events $\omega \to \pi^0\gamma$ in the peak is

$$N_{\omega\to\pi^0\gamma} = 55340 \pm 363. \tag{40}$$

The reconstruction efficiency for these events is determined with Monte Carlo events of the type $\overline{p}p \to \pi^0\omega(\omega \to \pi^0\gamma) \to 5\gamma$. Out of 53,436 generated MC events, $N_{\omega\to\pi^0\gamma} = 12,770 \pm 120$ survive the cuts and the reconstruction efficiency therefore is

$$\varepsilon_{\omega\to\pi^0\gamma} = (23.9 \pm 0.2)\%. \tag{41}$$

To see the $\omega \to \eta\gamma$ events, events with at least one entry on the $\pi^0$ peak are rejected. However, the cut window defined in eqn. 26 has been increased here from 30 to 40 MeV. This cut helps to reduce the background contribution from $\pi^0\pi^0\eta$, which has often at least one $\gamma$ near the $\pi^0$ peak.

The main problem, however, is background from $\pi^0 a_2^0$ where $a_2^0 \to \pi^0\eta$. Consider the reaction $\overline{p}p \to \pi_A^0 a_2, a_2 \to \pi_B^0\eta$. If one photon $\gamma_1$ from $\pi_A^0$ is not detected while the second (detected) photon $\gamma_2$ together with the $\eta \to \gamma_3\gamma_4$ fall in the $\omega$ mass region ($\omega \to \gamma_2\gamma_3\gamma_4$), then the event fakes a perfect $\pi^0\omega(\omega \to \eta\gamma)$ event. This is shown in figure 40 where the invariant mass $m(\pi_B^0\gamma_3\gamma_4)$ is plotted for events where $\gamma_2$ lies in the kinematically allowed region for $\omega \to \eta\gamma_2$ ($|E_\gamma\ [\mathrm{MeV}] - 200| < 20$). The peak around 1320 MeV corresponds to $a_2 \to \pi_B^0\eta$. The hatched histogram shows the expected spectrum from MC $\omega \to \eta\gamma$ events. A new cut on $a_2$ is therefore introduced to reject these events which fake an $\omega \to \eta\gamma$ signal, rejecting every event for which

$$m(\pi_B^0\gamma_3\gamma_4)\ [\mathrm{MeV}] < 1350 \quad \text{and} \quad |E_{\gamma_2}\ [\mathrm{MeV}] - 200| < 20. \tag{42}$$

where the 3 $\gamma$'s are permutated. The 1350 MeV cut rejects $a_2$ events without significantly affecting the $\omega \to \eta\gamma$ events. This has been optimized by MC simulation.

The energy distribution of the 3 $\gamma$'s in the $\omega$ rest frame after the cuts on $\omega \to \pi^0\gamma$ and $a_2$ is shown in figure 41. The peak at 200 MeV corresponds to $\omega \to \eta\gamma$.

Next, remaining background from $6\gamma$ events and from $\eta\omega(\omega \to \pi^0\gamma$ has to be subtracted. The number of background events is:

$$\begin{array}{lcr} \pi^0\pi^0\pi^0 & : & 10 \\ \pi^0\pi^0\eta & : & 585 \\ \pi^0\eta\eta & : & 5 \\ \eta\omega(\omega \to \pi^0\gamma) & : & 99 \end{array} \tag{43}$$

The contributions from $\pi^0\pi^0\pi^0$ with 10 and from $\pi^0\eta\eta$ with 5 events are completely negligible. The energy distribution of the two other channels is shown in figure 41 by the hatched histogram. The resulting histogram after background subtraction is plotted in figure 42. The general form of the spectrum is in good

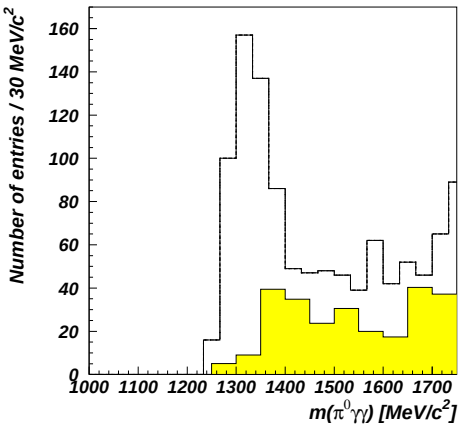


Figure 40: $m(\pi^0_B\gamma_3\gamma_4)$ *distribution. The hatched histogram shows the expected distribution from MC* $\omega \to \eta\gamma$ *events. The two histograms are not normalized and have a different binning. The peak in the data is due to* $a_2^0(1320) \to \eta\pi^0$.

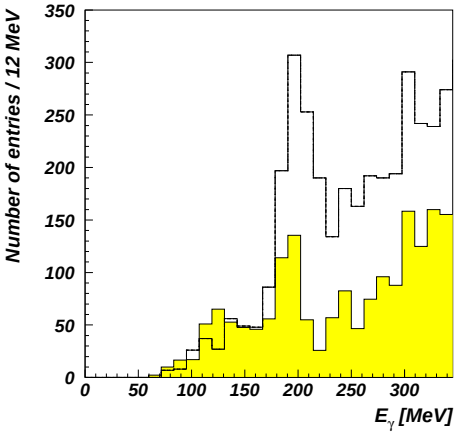


Figure 41: $E_\gamma$ *distribution for events which survive the* $\pi^0$ *and the* $a_2$ *cuts described in the text. A clear* $\eta$ *peak is observed around 200 MeV. The hatched histogram shows the background contribution from* $\pi^0\pi^0\eta$ *and* $\eta\omega, \omega \to \pi^0\gamma$.

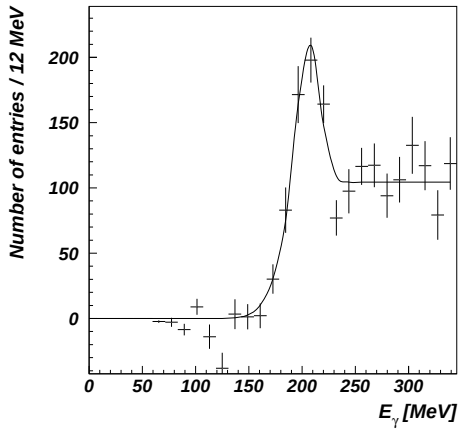


Figure 42: *Same as in figure 41 but after background subtraction. The fit is described in the text.*

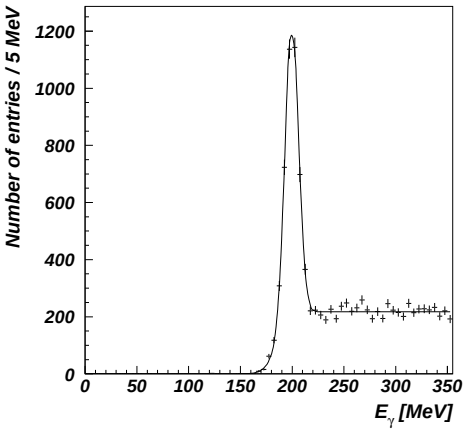


Figure 43: $E_\gamma$ *distribution in the* $\omega$ *rest frame for* $\pi^0\omega, \omega \to \eta\gamma$ *MC events. The same cuts as for data events have been applied.*

agreement with the expected $\omega \to \eta\gamma$ spectrum (figure 43). Almost no events are seen below 170 MeV and the spectrum is completely flat above 250 MeV. This indicates that the background and the applied cuts are well understood. However, the $\eta$ peak in the data histogram is much wider than expected from MC $\omega \to \eta\gamma$ simulation. This is a first indication of a contribution from the broad $\rho$ which enlarges the $\eta$ peak. To count the number of $\omega \to \eta\gamma$ events in the resulting histogram, the fit described in section 6.1 is used[6]. The following parameters for the Gaussian are found

$$\begin{aligned} E &= (206.1 \pm 4.4) \text{ MeV} \\ \sigma &= (10.46 \pm 2.82) \text{ MeV} \\ A &= (107.1 \pm 16.6) \text{ events/bin}, \end{aligned} \tag{44}$$

which yields the number of $\omega \to \eta\gamma$ events:

$$N_{\omega\to\eta\gamma} = 233 \pm 72. \tag{45}$$

As it was mentioned above, a proper $\omega \to \eta\gamma$ branching ratio cannot be derived from this number due to the unknown $\rho$ contribution. However, it is done here to gain a first impression of the behaviour of the $\rho - \omega$ mixing. Note that the 'branching ratio' calculated here is therefore *not* a correct determination of the $\omega \to \eta\gamma$ branching ratio and that the oucome will not have further impacts in this work.

The $\omega \to \eta\gamma$ reconstruction efficiency is estimated with weighted $\pi^0\eta\gamma$ events to include the $\omega \to \eta\gamma$ angular distribution. The reconstruction efficiency is

$$\varepsilon_{\omega\to\eta\gamma} = (15.0 \pm 0.5)\%. \tag{46}$$

A ratio of the two branching ratios $\omega \to \eta\gamma$ and $\omega \to \pi^0\gamma$ can be calculated using the number of $\omega \to \pi^0\gamma$ events from eqn. 40 and the $\omega \to \pi^0\gamma$ reconstruction efficiency from eqn. 41:

$$\frac{BR(\omega \to \eta\gamma)}{BR(\omega \to \pi^0\gamma)} = \frac{N_{\omega\to\eta\gamma}}{N_{\omega\to\pi^0\gamma}} \cdot \frac{\varepsilon_{\omega\to\pi^0\gamma}}{\varepsilon_{\omega\to\eta\gamma}} \cdot \frac{BR(\pi^0 \to 2\gamma)}{BR(\eta \to 2\gamma)} = (17.3 \pm 5.4) \times 10^{-3}. \tag{47}$$

By multiplying this with the $\omega \to \pi^0\gamma$ branching ratio [11] the $\omega \to \eta\gamma$ branching ratio is obtained:

$$BR(\omega \to \eta\gamma) = (14.7 \pm 4.6) \times 10^{-4}. \tag{48}$$

The assumption that no $\rho$ is produced coherently in $\overline{p}p \to \pi^0\rho$ leads to an $\omega \to \eta\gamma$ branching ratio which is a factor of 2.3 larger and *completely* inconsistent with the measurement in section 6.1, thus proving that the coherent contribution from $\rho$ cannot be neglected in $\pi^0\omega$.

[6]Note that a simple subtraction and integration as in section 6.1 is not possible here due to the broad combinatorial background.

## 6.3 Upper Limit for the Branching Ratio $\omega \to 3\gamma$

In this section, an upper limit for the decay branching ratio of $\omega \to 3\gamma$ where $\omega$ decays directly to $3\gamma$ is derived. This process is similar to the decay of *Ortho*positronium into $3\gamma$ [17] [18] and has not been observed so far. Two-photon annihilation is allowed only for $e^+e^-$ pairs in the $^1S_0$ state. When the annihilation into two photons is ruled out by $C$-Paritity conservation in $^3S_1$ decay, three-photon annihilation is the process of lowest order possible. It is assumed here that the process $\omega \to 3\gamma$ is purely electromagnetic (ignoring form-factors) and therefore has the same dynamics as the Orthopositronium decay.

The energy distribution of the three photons has been calculated in ref. [18]. The explicit formula for the energy distribution of a photon is

$$\begin{aligned} I(p) &= 2 \cdot \left\{ \tfrac{p(m-p)}{(2m-p)^2} - \tfrac{2m(m-p)^2}{(2m-p)^3} \log \tfrac{m-p}{m} \right. \\ &\quad \left. + \tfrac{2m-p}{p} + \tfrac{2m(m-p)}{p^2} \log \tfrac{m-p}{m} \right\}, \end{aligned} \tag{49}$$

where $I(p)$ denotes the intensity as a function of the momentum $p$ and $m$ is the mass of the electron, $m(e^-) = E_{tot}/2$. The intensity is plotted in fig. 44 as a function of $E_\gamma/E_{tot}$.

The photon spectrum varies linearly with energy except for energies near $E_{max} = E_{tot}/2$. Phase space generated MC $\omega \to 3\gamma$ events (fig. 45) show a very similar structure and are a good approximation to the expected energy distribution. Only the region above 350 MeV ($E_\gamma/E_{tot} > 0.45$) does not agree well with phase space distribution, but this region will be cut off (eqn. 50 below). One can therefore use phase space $\omega \to 3\gamma$ MC events to determine the reconstruction efficiency.

The decay process $\omega \to 3\gamma$ proceeds mainly through the intermediate particles $\pi^0$ and $\eta$. Both particles manifest themselves as bands in the $\omega \to 3\gamma$ Dalitz plot (figs. 20,21). To count the potential $\omega \to 3\gamma$ events, these two bands have to be cut off. In addition, background lying outside these bands has to be identified and rejected. The Dalitz plot from $\pi^0\omega$, figure 20, has less background events *outside* the two bands and is therefore used to determine an upper limit.

The main background contribution outside the bands stems from $\pi^0\pi^0\eta$. Background from $\pi^0\pi^0\pi^0$, which also contributes to $\pi^0\omega$, is negligible outside the $\omega \to \pi^0\gamma$ bands. The $\omega \to 3\gamma$ Dalitz plot for $\pi^0\pi^0\eta$ events is shown in figure 46. This background channel contributes with a total number of 1263 events to the $\pi^0\omega$ channel, which corresponds to 2% of all selected $\pi^0\omega$ events. The Dalitz plot is completely depleted in a triangle in the middle of the plot where the 3 $\gamma$'s have all energies $E_\gamma > 230$ MeV. This region is suitable for a determination of a decay upper limit, since no background subtraction has to be performed. This region was selected with the cut

$$234 \text{ MeV} < E_{\gamma_i} < 303 \text{ MeV}, \tag{50}$$

where the relation holds for all 3 $\gamma$'s ($i = 1, 2, 3$). The cut selects events in a region with the highest possible reconstruction efficiency without contaminating

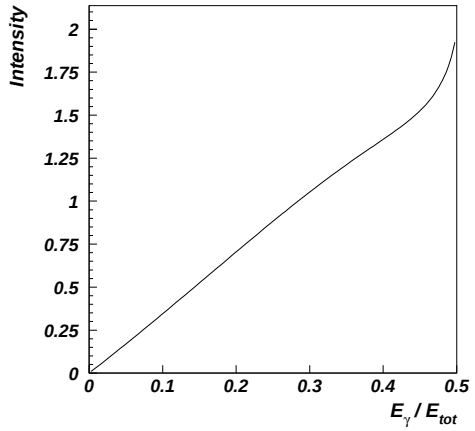


Figure 44: *$E_\gamma/E_{tot}$ for the theoretical energy spectrum of $e^+e^- \to 3\gamma$.*

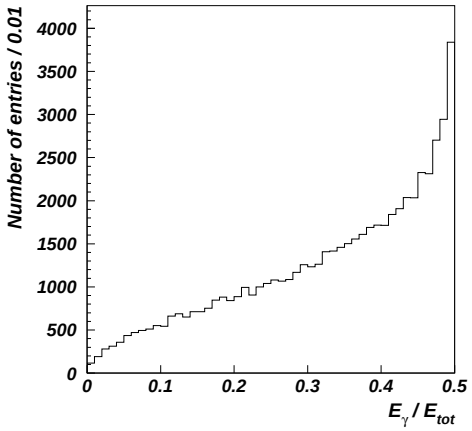


Figure 45: *$E_\gamma/E_{tot}$ for phase space $\omega \to 3\gamma$ events ($E_{tot} = m_\omega$).*

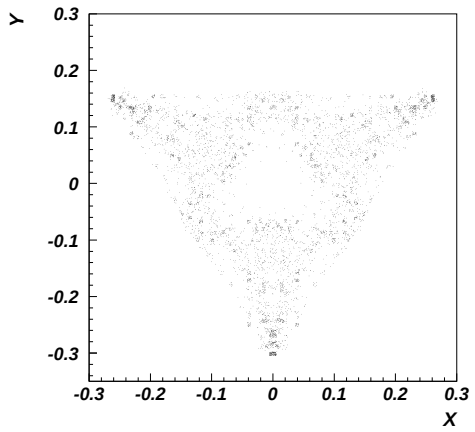


Figure 46: *$\omega \to 3\gamma$ MC Dalitz plot for bakckground events from $\pi^0\pi^0\eta$ in the $\pi^0\omega$ channel. The total contamination is 1263 events.*

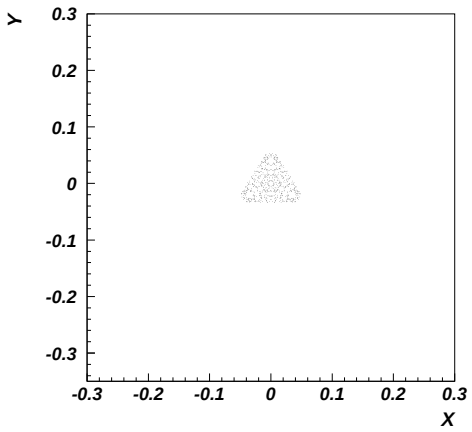


Figure 47: *$\omega \to 3\gamma$ Dalitz plot for MC phase space distributed $\omega \to 3\gamma$ events after the cut described in the text.*

the region with background from $\pi^0\pi^0\eta$.

The result is shown in figure 47 where the cut has been applied to MC $\omega \to 3\gamma$ events. Out of 20,000 generated $\omega \to 3\gamma$ events, $114 \pm 11$ survive the cuts and the reconstruction efficiency therefore is

$$\varepsilon_{\omega\to 3\gamma} = (0.57 \pm 0.06)\%. \tag{51}$$

In the $\pi^0\omega$ data Dalitz plot, shown in fig. 20, only one event survives this cut and is a potential $\omega \to 3\gamma$ event[7]. To obtain an upper limit at 95% confidence level for the number of observed events, one has to sum over the Poisson probabilities and find the minimum integer number $N$ for which

$$\sum_{k=0}^{N} \frac{\lambda^k}{k!} e^{-\lambda} > 0.95, \tag{52}$$

where $\lambda$ denotes the number of observed events, $\lambda = 1$. This equation holds for $N \geq 3$. The number of observed events is therefore

$$N_{\omega\to 3\gamma} < 3 \text{ at } 95\%\ CL. \tag{53}$$

One can now calculate the upper limit for the branching ratio $BR(\omega \to 3\gamma)$, excluding $\eta$ and $\pi^0$ intermediate states, using the decay $\omega \to \pi^0\gamma$, measured in section 6.2, for normalization:

$$\begin{aligned} BR(\omega \to 3\gamma) &< \frac{N_{\omega\to 3\gamma}}{\varepsilon_{\omega\to 3\gamma}} \cdot \frac{\varepsilon_{\omega\to\pi^0\gamma}}{N_{\omega\to\pi^0\gamma}} \cdot BR(\omega \to \pi^0\gamma) \\ &= 1.9 \times 10^{-4} \text{ at } 95\%\ CL. \end{aligned} \tag{54}$$

An upper limit for this reaction has previously been published by Prokoshkin and Samoilenko in ref. [19]. They obtain $BR(\omega \to 3\gamma) < 2 \times 10^{-4}$ at 90% $CL$. However, a comparision with the value in eqn. 54 is not possible since they do not give the analysis method.

Anyway, the present analysis yields a lower upper-limit with an even higher confidence level.

[7]Note that although 6 entries are visible in the inner triangle of the $\pi^0\omega$ Dalitz plot, these entries stem from only one event since every event is entered 6 times.

## 6.4 $\rho - \omega$ Mixing

The analysis of the $\pi^0\omega$ channel (section 6.2) clearly shows that coherent contribution from $\rho$ cannot be neglected, at least for $\overline{p}p \to \pi^0\omega$. But, since this work treats two different production channels for $\omega$ and hence two different relative contributions from $\rho$, it is possible to gain more information about the behaviour of the $\rho-\omega$ mixing by combining the two channels and giving a consistent picture concerning the radiative $\omega$ decay to $\eta\gamma$.

### 6.4.1 Theory of $\rho - \omega$ Mixing

The theory of the $\rho - \omega$ mixing presented here was suggested by Coleman and Glashow in ref. [20] and later in more details in ref. [21]. They explain the distortion of the $\rho \to \pi^+\pi^-$ line-shape due to the small $\omega \to \pi^+\pi^-$ admixture. Recent theoretical papers (e.g. refs. [22] or [23]) introduce additional quark-loops and momentum dependence of the mixing matrix element, but which produce only small corrections and are not considered here. The theory applies to $\rho$ and $\omega$ states which are produced coherently. This is the case for $\overline{p}p$ annhiliation. Consider two decoupled states

$$\rho = \begin{pmatrix} 1 \\ 0 \end{pmatrix}, \quad \omega = \begin{pmatrix} 0 \\ 1 \end{pmatrix}, \tag{55}$$

and $\psi \equiv (\rho, \omega)^T$. The Hamiltonian is then given by

$$H = \begin{pmatrix} m_\rho - i\Gamma_\rho/2 & 0 \\ 0 & m_\omega - i\Gamma_\omega/2 \end{pmatrix}, \tag{56}$$

from which, with $H\psi = E\psi$, the eigenvalues of the decoupled states can be derived:

$$\begin{aligned} E_\rho &= m_\rho - i\Gamma_\rho/2, \\ E_\omega &= m_\omega - i\Gamma_\omega/2. \end{aligned} \tag{57}$$

Now consider the $\rho - \omega$ coupling through a photon. The coupling parameter is $\delta$. The new Hamiltonian $H'$ is of the form

$$H' = \begin{pmatrix} m_\rho - i\Gamma_\rho/2 & -\delta \\ -\delta & m_\omega - i\Gamma_\omega/2 \end{pmatrix}, \tag{58}$$

and hence,

$$H'\psi' = E'\psi'. \tag{59}$$

Coleman and Glashow [20] relate the matrix element $\delta$ to the $SU(3)$ breaking mass splitting of the known mesons and baryons states and predict

$$\delta \approx 2.5 \text{ MeV}. \tag{60}$$

The eigenstates $\rho'$ and $\omega'$ can be calculated using first order perturbation theory:

$$\begin{aligned} \rho' &= \rho - \frac{\delta}{E_\rho - E_\omega} \cdot \omega, \\ \omega' &= \omega - \frac{\delta}{E_\omega - E_\rho} \cdot \rho, \end{aligned} \tag{61}$$

which is verified by inserting eqn. 61 into eqn. 59 and neglecting the $\delta^2$ terms. With the definition $\Delta \equiv m_\rho - m_\omega - i/2(\Gamma_\rho - \Gamma_\omega)$ and the eigenvalues $E_\rho$ and $E_\omega$ from eqn. 57, the physical eigenstates are

$$\begin{aligned} \rho' &= \rho - \frac{\delta}{\Delta} \cdot \omega, \\ \omega' &= \omega + \frac{\delta}{\Delta} \cdot \rho. \end{aligned} \tag{62}$$

The amplitude $S$ for the reaction $\overline{p}p \to X(\rho - \omega) \to X\eta\gamma$ can now be given in terms of mixed states:

$$\begin{aligned} S &= (A_\rho, A_\omega) \cdot (m - H')^{-1} \cdot \begin{pmatrix} T_\rho \\ T_\omega \end{pmatrix} \\ &= (A_\rho, A_\omega) \cdot \begin{pmatrix} m - m_\rho + i\Gamma_\rho/2 & \delta \\ \delta & m - m_\omega + i\Gamma_\omega/2 \end{pmatrix}^{-1} \cdot \begin{pmatrix} T_\rho \\ T_\omega \end{pmatrix}, \end{aligned} \tag{63}$$

where $A$ is the production and $T$ the decay amplitude of the two mesons. With the abbreviations $P_\rho \equiv m - m_\rho + i\Gamma_\rho/2$ and $P_\omega \equiv m - m_\omega + i\Gamma_\omega/2$, eqn. 63 becomes

$$\begin{aligned} S &= (A_\rho, A_\omega) \cdot \begin{pmatrix} P_\rho & \delta \\ \delta & P_\omega \end{pmatrix}^{-1} \cdot \begin{pmatrix} T_\rho \\ T_\omega \end{pmatrix} \\ &= (A_\rho, A_\omega) \cdot \frac{1}{P_\rho P_\omega - \delta^2} \begin{pmatrix} P_\omega & -\delta \\ -\delta & P_\rho \end{pmatrix} \cdot \begin{pmatrix} T_\rho \\ T_\omega \end{pmatrix} \\ &\overset{\delta^2 \simeq 0}{\simeq} \frac{1}{P_\rho P_\omega} (A_\rho P_\omega - A_\omega \delta, -A_\rho \delta + A_\omega P_\rho) \begin{pmatrix} T_\rho \\ T_\omega \end{pmatrix} \\ &= \frac{1}{P_\rho P_\omega} (A_\rho P_\omega T_\rho - A_\omega \delta T_\rho - A_\rho \delta\ T_\omega + A_\omega P_\rho T_\omega) \\ &= \frac{A_\rho T_\rho}{P_\rho} \left(1 - \frac{A_\omega}{A_\rho} \frac{\delta}{P_\omega}\right) + \frac{A_\omega T_\omega}{P_\omega} \left(1 - \frac{A_\rho}{A_\omega} \frac{\delta}{P_\rho}\right). \end{aligned} \tag{64}$$

$A_{\rho,\omega}$ and $T_{\rho,\omega}$ are complex amplitudes with unknown phases $\alpha$ between $A_\rho$ and $A_\omega$ and $\phi$ between $T_\rho$ and $T_\omega$. With these angles, the total transition amplitude $S$ may be written as

$$S = \frac{|A_\rho||T_\rho|}{P_\rho} \left(1 - \frac{|A_\omega|}{|A_\rho|} \frac{e^{i\alpha}\delta}{P_\omega}\right) + e^{i\alpha} e^{i\phi} \frac{|A_\omega||T_\omega|}{P_\omega} \left(1 - \frac{|A_\rho|}{|A_\omega|} \frac{e^{-i\alpha}\delta}{P_\rho}\right). \tag{65}$$

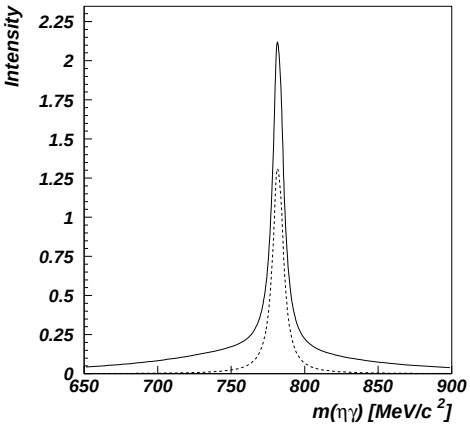


Figure 48: $|S|^2$ *for* $\overline{p}p \to \pi^0(\rho-\omega) \to \pi^0\eta\gamma$ *for* $\alpha = \phi = 0$. *The dashed line shows the line-shape with no* $\rho$ *admixture.*

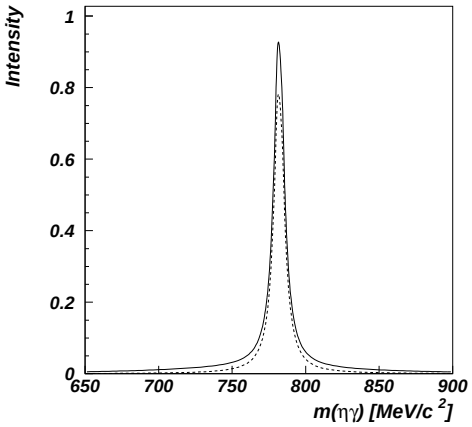


Figure 49: $|S|^2$ *for* $\overline{p}p \to \eta(\rho-\omega) \to \eta\eta\gamma$ *for* $\alpha = \phi = 0$. *The dashed line shows the line-shape with no* $\rho$ *admixture.*

The intensity for this amplitude is $I = |S|^2$. For $\delta = 0$, i.e. if no coupling of the two mesons to the photon is considered, $S$ reduces to a sum of two Breit-Wigner functions. The amplitudes $A$ and $T$ are given by

$$\begin{aligned} A_{\rho,\omega} &= \sqrt{BR(\overline{p}p \to \rho,\omega)}\ , \\ T_{\rho,\omega} &= \sqrt{\Gamma_{\rho,\omega\to xy}} = \sqrt{BR(\rho,\omega \to xy)\cdot\Gamma_{\rho,\omega}}\ . \end{aligned} \tag{66}$$

In $(\rho-\omega) \to \pi^+\pi^-$, the isospin violating decay amplitude $T_\omega = T(\omega \to \pi^+\pi^-)$ can be neglected and only the first term of the production amplitude $S = S(\pi^+\pi^-)$ can be taken into account. In that case, one has to deal with only *one* relative phase $e^{i\phi}$, which simplifies the situation. This is not possible for the reaction $(\rho-\omega) \to \eta\gamma$ where none of the amplitudes is sufficiently small. One therefore has to use $S$ from eqn. 65 with the two *a priori* unknown phases $\alpha$ and $\phi$.

However, the production phase $\alpha$ is expected to be near zero for similar production mechanisms [24]. In $e^+e^-$ annihilation to $(\rho-\omega) \to \pi^+\pi^-$ [7], where the second term in eqn. 65 can be neglected, the phase $\phi$ can be either 0° or 180° (by time reversal arguments [6]), corresponding to constructive, respectively destructive $\rho-\omega$ interference, and two solutions for the branching ratios are possible. In photoproduction of $(\rho-\omega) \to \eta\gamma$ [6] the phase $\alpha$ is set to 0° and again two solutions $\phi = 0°$ or $\phi = 180°$ are possible for the branching ratios. The solution $\phi = 0°$ is predicted by the quark model.

The same approximation ($\alpha \equiv 0°$) is made here. It has been tested with the MC method presented in section 6.4.2 that any production angle $\alpha$ is compatible with the data as long as $\phi \sim \alpha$. This shows that the data is only sensitive to the relative phase $e^{i(\alpha+\phi)}$ between the two Breit-Wigner functions in eqn. 65 and $\delta$

is too small for a determination of both phases. Thus constructive interference means that $\phi \sim \alpha$.

The $|S|^2$ for the two channels $\pi^0(\rho-\omega)$ and $\eta(\rho-\omega)$ are plotted in figures 48 and 49 where the production and decay branching ratios were taken from refs. [13] and [16] and $\alpha = \phi = 0$. The line-shape for $\eta(\rho-\omega)$ is almost a simple Breit-Wigner while for $\pi^0(\rho-\omega)$ the $\rho$ contributes significantly.

### 6.4.2 Coupled Analysis of Both Channels

The transition amplitude for $\rho-\omega$ mixing, derived in section 6.4.1, is now used to include the interference in the description of the data. The idea is to produce the number of observed events $(\rho-\omega) \to \eta\gamma$ in both channels $\pi^0(\rho-\omega)$ and $\pi^0(\rho-\omega)$ events as a function of $BR(\omega \to \eta\gamma)$, $BR(\rho \to \eta\gamma)$ and the relative decay phase $\phi$. The production branching ratios in $A$ were *not* treated as free parameters since they are known [11] [13]. The simulation is based on Monte Carlo data. The following event types are generated with CBGEANT according to phase space:

- $\pi^0\eta\gamma$ events to simulate the channel $\pi^0(\rho-\omega)$ (105,000 generated events).
- $\eta\eta\gamma$ events to simulate the channel $\eta(\rho-\omega)$ (100,000 generated events).

These events are weighted in the $\eta\gamma$ system with the dynamical function $|S|^2$ which includes the branching ratios $BR(\rho \to \eta\gamma)$ and $BR(\omega \to \eta\gamma)$ in the amplitudes $T_\rho$ and $T_\omega$, respectively. In addition, each MC event $i$ is weighted with the decay angular distribution $w(\cos\theta_i)$ given in eqn. 16. Hence the total number of MC events after weighting is

$$N_{eff}^{MC} = \sum_{i=1}^{N^{MC}} |S_i|^2 \cdot w(\cos\theta_i), \tag{67}$$

where $N^{MC}$ denotes the number of MC events before weighting. Note that in the case of no $\rho$ admixture, $|S|^2$ reduces to

$$|S_i|^2 \text{ (no } \rho) = |P_{\omega,i}|^2 \cdot BR(\overline{p}p \to \pi, \eta\omega) \cdot BR(\omega \to \eta\gamma) \cdot \Gamma_\omega \cdot w(\cos\theta_i), \tag{68}$$

where $P_\omega$ is the simple Breit-Wigner function. This is used to normalize the hole MC data set. The overall normalization is done such that $N_{eff}^{MC}$ equals the number of expected $\pi^0\omega$ and $\eta\omega$ events, where $\omega \to \eta\gamma$, present in the all neutral data sample, i.e.

$$\begin{aligned} N_{exp}^{\pi^0\omega} &= N_{\overline{p}p} \cdot BR(\overline{p}p \to \pi^0\omega) \cdot BR(\omega \to \eta\gamma), \\ N_{exp}^{\eta\omega} &= N_{\overline{p}p} \cdot BR(\overline{p}p \to \eta\omega) \cdot BR(\omega \to \eta\gamma). \end{aligned} \tag{69}$$

The number of MC events after weighting is scaled to the expected number of events with the factor $f$,

$$
\begin{aligned}
f &= \frac{N_{exp}^{\pi^0\omega,\eta\omega}}{N_{eff}^{MC}} \\
&= \frac{N_{\overline{p}p} \cdot BR(\overline{p}p \to \pi^0,\eta\omega) \cdot BR(\omega \to \eta\gamma)}{\sum_{i=1}^{N^{MC}} |P_{\omega,i}|^2 \cdot BR(\overline{p}p \to \pi,\eta\omega) \cdot BR(\omega \to \eta\gamma) \cdot \Gamma_\omega \cdot w(\cos\theta_i)} \\
&= \frac{N_{\overline{p}p}}{\sum_{i=1}^{N^{MC}} |P_{\omega,i}|^2 \cdot \Gamma_\omega \cdot w(\cos\theta_i)}.
\end{aligned}
\tag{70}
$$

Note that the normalization constant $f$ is therefore independent of any branching ratio. The number of simulated $\omega \to \eta\gamma$ events is now extracted in the following steps:

1. The generated MC events are then passed through the offline analysis and kinematic fit routine as described in section 3. The same cuts as for data events are applied. The energy and momenta of the surviving events are stored as well as the original MC values.

2. The $\eta\gamma$ system of every surviving event is now weighted with the amplitude $f\,|S|^2\,w(\cos\theta_i)$ including both $\rho$ and $\omega$ contributions. The two decay branching ratios and the mixing angle $\phi$ are given as an *input* to calculate $|S|^2$. Note that the original MC energies and momenta are used to weight the events.

3. To extract the number of $\eta\gamma$ events, the same analysis method and cuts as for data events are applied (see section 6.1 and 6.2).

The production and decay branching ratios used for the simulation are:

$$
\begin{aligned}
BR(\overline{p}p \to \pi^0\omega) &= (5.73 \pm 0.47) \times 10^{-3}\ [13], \\
BR(\overline{p}p \to \pi^0\rho) &= (1.72 \pm 0.27) \times 10^{-2}\ [25], \\
BR(\overline{p}p \to \eta\omega) &= (1.51 \pm 0.12) \times 10^{-2}\ [13], \\
BR(\overline{p}p \to \eta\rho) &= (5.7 \pm 1.5) \times 10^{-3}.
\end{aligned}
\tag{71}
$$

The value for $\overline{p}p \to \eta\rho$ given here is the weighted average from available data in ref. [16] and the error is the typical error on the individual measurements and reflects the experimental situation[8]. These branching ratio are called 'table values' in the following.

Since these branching ratios all have an error, the total weight $|S|^2$ too is not error free. The error on a bin in a histogram filled with these weighted events is calculated as explained in appendix C, including the error on $|S|^2$.

The numbers of *observed* $(\rho - \omega) \to \eta\gamma$ events $N_{obs}$ in both production channels (see section 6.1 and 6.2),

[8]However, this error has very little effect on the determination of the mixing parameters.

$$\begin{aligned} N_{obs}(\pi^0(\rho-\omega)\to\pi^0\eta\gamma) &= 233\pm 72, \\ N_{obs}(\eta(\rho-\omega)\to\eta\eta\gamma) &= 111\pm 17, \end{aligned} \tag{72}$$

shall now be compared with the numbers of *simulated* events $N_{sim}$.

In a first step, to check for consistency with previous measurements and to see if the number of observed events in the $\pi^0\omega$ channel can be explained with $\rho-\omega$ mixing, the two decay branching ratios for $\omega\to\eta\gamma$ and $\rho\to\eta\gamma$ are fixed to their table values[9] [11]

$$\begin{aligned} BR(\omega\to\eta\gamma) &= (8.3\pm 2.1)\times 10^{-4}, \\ BR(\rho\to\eta\gamma) &= (3.8\pm 0.7)\times 10^{-4}, \end{aligned} \tag{73}$$

and only the relative phase $\phi$ is varied. The result is shown in figure 50. The number of simulated events in the $\pi^0\omega$ channel (triangles) and $\eta\omega$ channel (circles) are shown as a function of the relative phase $\phi$, which is varied in steps of 18° from $-180°$ to 180°. The error is calculated with the method presented in appendix C. The hatched regions give the $1\sigma$ range (68 % *CL*) of the observed number of events in the $\pi^0(\rho-\omega)$ and the $\eta(\rho-\omega)$ channel, respectively.

The number of simulated events in the $\pi^0(\rho-\omega)$ channel varies rapidly with $\phi$ (from 64 events at $-155°$ to 189 events at 15°) and reaches the $1\sigma$ range only for $\phi\approx 0$. The data therefore clearly favours *constructive* $\rho-\omega$ interference. However, the MC simulation always underestimates the number of observed events in the $\pi^0(\rho-\omega)$ channel (233 events) which suggests a *larger* branching ratio of $\rho\to\eta\gamma$.

The number of simulated events in the $\eta(\rho-\omega)$ channel does not depend strongly on $\phi$ and stays always, except for $\phi\approx -150°$, within $1\sigma$ of the observed number of events. For $\phi\approx 0$, preferred by the $\pi^0(\rho-\omega)$ channel, the MC simulation, with the table value of $\omega\to\eta\gamma$ [5] as a fixed parameter, produces a larger number of events than observed. Thus a *lower* $\omega\to\eta\gamma$ branching ratio than the table value is preferred.

As a general result, it is noted that the observed numbers of events in both channels are consistent with the table values for $BR(\omega\to\eta\gamma)$ and $BR(\rho\to\eta\gamma)$ for a relative phase $\phi\approx 0$.

In a second step, it is tried to fit the $\rho$ and $\omega$ decay branching ratios and the relative phase $\phi$ to the data. The simulation method, which is very time consuming, does not permit the continuous variation of the parameters. The only practical method is to vary the three parameters in fixed steps and store the number of events as well as the errors in a table for each triplet of parameter. To judge whether a given set of parameters provides a good description of the data, the $\chi^2$ between data and MC

$$\chi^2 \equiv \left(\frac{(N_{obs}-N_{sim})^2}{\sigma_{obs}^2+\sigma_{sim}^2}\right)_{\pi^0(\rho-\omega)} + \left(\frac{(N_{obs}-N_{sim})^2}{\sigma_{obs}^2+\sigma_{sim}^2}\right)_{\eta(\rho-\omega)} \tag{74}$$

[9] The branching ratio for $\rho\to\eta\gamma$ refers to the solution with constructive interference, while the branching ratio for $\omega\to\eta\gamma$ is measured 'model independent'.

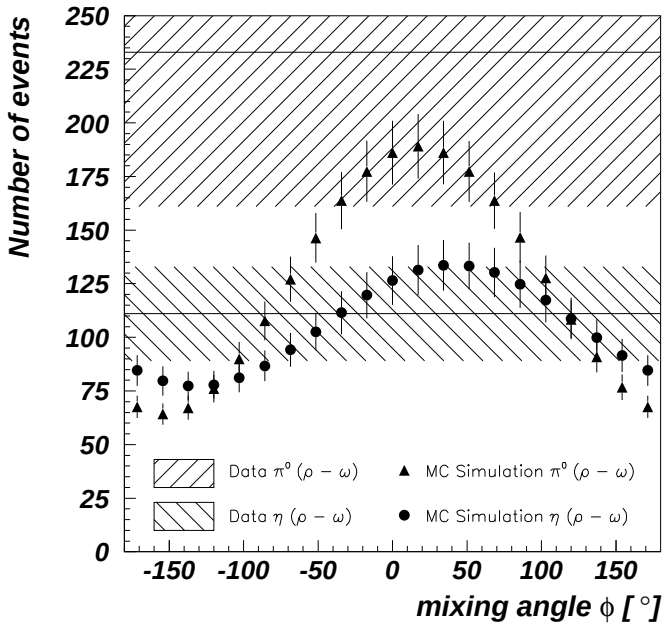


Figure 50: *Comparison Data-MC. For the MC simulation, the decay branching ratios for $\omega \to \eta\gamma$ and $\rho \to \eta\gamma$ are fixed to their table values [11]. The two hatched regions show the $1\sigma$ range of the number of observed data events (horizontal lines). The number of observed events in the $\pi^0(\rho - \omega)$ channel can only be explained with a relative phase $\phi \approx 0°$, thus $(\rho - \omega)$ interference is constructive.*

is calculated, where $\sigma^2_{sim}$ includes the error on branching ratios in eqn. 71. To find the best description, the set of parameters for which $\chi^2$ is minimum has to be found. Note that the $\chi^2$ defined here does not follow a $\chi^2$ distribution since three parameters are fitted with only two data points. Thus the errors on the three parameters cannot be estimated with the $\chi^2$ method.

Such a table has been generated with

$$\begin{aligned} BR(\omega \to \eta\gamma) &: \text{11 steps from 0.5 to 1.5 (} \times \text{ table value), step size 0.1,} \\ BR(\rho \to \eta\gamma) &: \text{11 steps from 1.0 to 3.0 (} \times \text{ table value), step size 0.2,} \\ \phi &: \text{11 steps from } -50° \text{ to } 50°, \text{ step size } 10°. \end{aligned} \tag{75}$$

This gives a total number of 1331 combinations of parameters. The minimum $\chi^2$ is found at the lattice point

$$\begin{aligned} BR(\omega \to \eta\gamma) &: 0.8 \text{ (} \times \text{ table value),} \\ BR(\rho \to \eta\gamma) &: 2.4 \text{ (} \times \text{ table value),} \\ \phi &: -20°. \end{aligned} \tag{76}$$

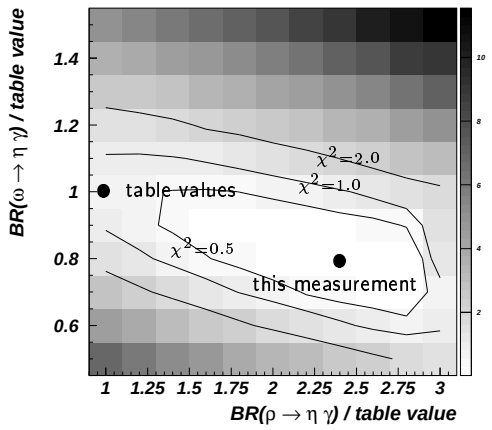


Figure 51: $\chi^2$ *distribution for* $\phi = -20°$. *The minimum* $\chi^2$ *is given by the circle 'this measurement'. The area with low* $\chi^2$ *shows the allowed region for the combination of the two branching ratios.*

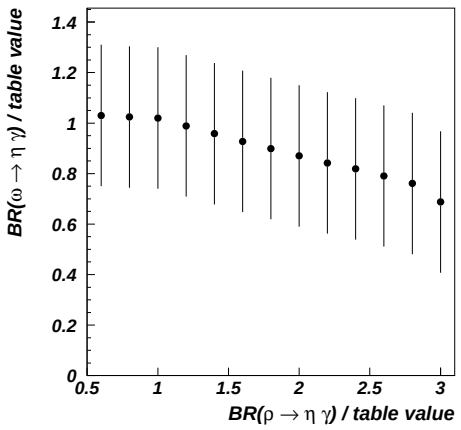


Figure 52: $BR(\omega \to \eta\gamma)$ *as a function of the branching ratio* $BR(\rho \to \eta\gamma)$. *The* $BR(\omega \to \eta\gamma)$ *decreases with increasing* $\rho \to \eta\gamma$ *contribution.*

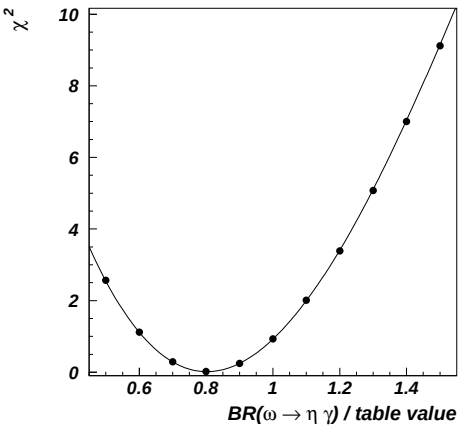


Figure 53: $\chi^2$ *distribution as a function of* $BR(\omega \to \eta\gamma)$ *for* $\phi = -20°$ *and* $BR(\rho \to \eta\gamma) = 2.4 \times$ *table value. The fit shows a third order polynomial. The minimum* $\chi^2$ *is found at* $BR(\omega \to \eta\gamma) = 0.80 \times$ *table value.*

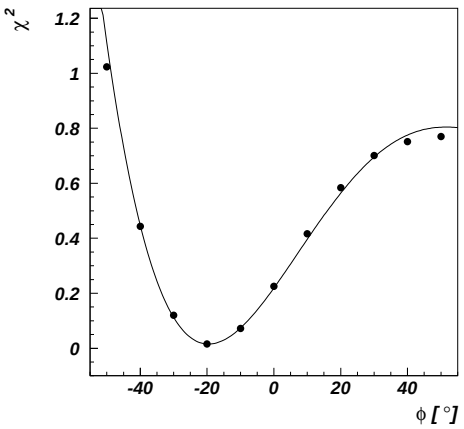


Figure 54: $\chi^2$ *distribution as a function of* $\phi$ *for* $BR(\omega \to \eta\gamma) = 0.8 \times$ *table value and* $BR(\rho \to \eta\gamma) = 2.4 \times$ *table value. The fit shows a forth order polynomial. The minimum* $\chi^2$ *is found at* $\phi = -18°$.

The $\chi^2$ distribution as a function of the two branching ratios is shown in figure 51 for $\phi = -20°$. The combination of branching ratios at $\chi^2_{min}$ is labelled with 'this measurement'. A region of equally good solutions around $\chi^2_{min}$ in the center of the plot is observed. Figure 51 shows the general features of the coupled analysis:

- The branching ratio $BR(\rho \to \eta\gamma)$ is not well determined by the present analysis.
- The branching ratio $BR(\omega \to \eta\gamma)$ is not very sensitive on $BR(\rho \to \eta\gamma)$ but decreases slightly with increasing $BR(\rho \to \eta\gamma)$. This is shown in figure 52 where the branching ratio $BR(\omega \to \eta\gamma)$ with the lowest $\chi^2$ has been plotted for every branching ratio $BR(\rho \to \eta\gamma)$.
- The combination of branching ratios from previous measurements (marked with 'table values') lies within the region of low $\chi^2$'s ($\chi^2 < 1$). Although a larger branching ratio $\rho \to \eta\gamma$ is preferred by the present analysis, the error is quite large (see below).

The one-dimensional $\chi^2$ distributions for $BR(\omega \to \eta\gamma)$ and for $\phi$ are shown in figures 53 and 54, respectively, where the other two parameters were fixed to the values given in eqn. 76 (best values). To determine the position of lowest $\chi^2$, the two plots are fitted with polynomials. This is not done for $BR(\rho \to \eta\gamma)$ since the $\chi^2$ distribution is so flat that a fit will not improve the measurement. The following values have a minimum $\chi^2$:

$$\begin{aligned} BR(\omega \to \eta\gamma) &: 0.80\ (\times \text{ table value}), \\ \phi &: -18°. \end{aligned} \tag{77}$$

To estimate the errors on these values and on $BR(\rho \to \eta\gamma)$, the measured numbers of events, as given in eqn. 72, are varied within the errors and the whole coupled analysis is redone with this new set of parameters. The values found by the fit are summarized in table 6.

| $N(\pi^0\omega)$ | $N(\eta\omega)$ | $BR(\rho \to \eta\gamma)$ | $BR(\omega \to \eta\gamma)$ | $\phi$ |
|---|---|---|---|---|
| upper limit | upper limit | $> 3$ | 1 | $25°$ |
| upper limit | lower limit | $> 3$ | 0.6 | $-5°$ |
| lower limit | upper limit | 0.6 | 1.0 | $40°$ |
| lower limit | lower limit | 1.4 | 0.8 | $-45°$ |

Table 6: *Error estimation for the coupled fit. The two lefthand columns give the input to the coupled fit. Lower/upper limit means that the error is subtracted/added to the experimentally observed number of events. The result of the coupled channel fit is given in the righthand three columns. The branching ratios are given in terms of table values.*

The lowest and the highest values found by this method are taken as the lower and upper error for the best values. For the determination of the lower error for $BR(\rho \to \eta\gamma)$, a second table of simulated number of events was generated in the range of 0.5 to 1.5 ($\times$ table value) for $BR(\rho \to \eta\gamma)$ while the other two parameters were varied as given in eqn. 75. Since the upper error for $\rho \to \eta\gamma$ lies outside the generated table, it is assumed that the errors on $\rho \to \eta\gamma$ are symmetric. With this error estimation, the result of the coupled channel fit is:

$$\begin{aligned} BR(\rho \to \eta\gamma) &= (2.4 \pm 1.8)\ (\times \text{ table value}), \\ BR(\omega \to \eta\gamma) &= (0.80 \pm 0.20)\ (\times \text{ table value}), \\ \phi &= (-18^{+58}_{-27})^\circ, \end{aligned} \tag{78}$$

or explicitly:

$$\begin{aligned} BR(\rho \to \eta\gamma) &= (9.1 \pm 6.8) \times 10^{-4}, \\ BR(\omega \to \eta\gamma) &= (6.6 \pm 1.7) \times 10^{-4}, \\ \phi &= (-18^{+58}_{-27})^\circ. \end{aligned} \tag{79}$$

The $\omega \to \eta\gamma$ branching ratio given here is fully consistent with $BR(\omega \to \eta\gamma) = (7.05 \pm 1.19) \times 10^{-4}$ measured in section 6.1 assuming no $\rho$ contribution in $\overline{p}p \to \eta\omega \to \eta\eta\gamma$. The relative phase $\phi$ measured here is in excellent agreement with the determination of this angle in ref. [6]: $\phi = (-11 \pm 38)^\circ$ (in their constructive interference solution).

# 7 Discussion

The experimental results from the present work as well as the results from previous measurements are summarized in table 7.

The branching ratio $BR(\omega \to \eta\gamma)$ obtained with the coupled analysis of both channels is consistent with the one measured in the $\eta\omega$ channel assuming no $\rho$ contribution. The errors on the branching ratio obtained with the coupled analysis are somewhat larger due to the larger number of parameters. The value from the coupled fit *including* the coherent contribution from $\rho$, is slightly lower than the one for the $\eta\omega$ channel only, thus proving that a small coherent contribution from $\rho$ is present in the $\eta\omega$ channel. However, within the statistical errors, the $\rho$ contribution indeed can be neglected in $\eta\omega$ and the value measured in the $\eta\omega$ channel is therefore a good approximation of the $\omega \to \eta\gamma$ branching ratio.

The old standing ambiguity between constructive and destructive $\rho - \omega$ interference has been resolved in the present work since two different production channels for the two vector mesons are considered in the analysis, namely $\pi^0(\rho{-}\omega)$ and $\eta(\rho - \omega)$, and hence two different relative contributions from $\rho$. The coupled analysis reveals the $\rho - \omega$ mixing angle $\phi$ to be close to zero and $\rho - \omega$ mixing is therefore *constructive*. This is the first unambiguous measurement of the $\rho - \omega$ mixing parameters in the $\eta\gamma$ system.

The measured values for $BR(\omega \to \eta\gamma)$ agree well with the constructive interference solution of previous measurements. The relative decay phase $\phi$ given by Andrews *et al.* [6] is completely consistent with the value measured in the present work. Also, the value measured by Dolinsky *et al.* [7] is in excellent agreement with the present measurement, even though the relative phase $\phi$ was not a treated as free parameter but set to 0° or 180°, respectively. The branching ratio $BR(\omega \to \eta\gamma)$ reported by Alde *et al.* [5] is significantly higher than all other measurements, and inconsistent with the one by Andrews *et al.*. Alde *et al.* have used the charge-exchange reaction $\pi^- p \to \omega\ n$ at 38 GeV/$c$ as a source of $\omega$ mesons. Events at high momentum transfers $|\,t\,|$ were selected to reduce 'most' of the $\rho - \omega$ influence on the $\omega$ signal. However, no estimation of the remaining contamination of coherent background from $\pi^- p \to \rho\ n$ was made. Thus the higher branching ratio could originate from an unresolved contribution from $\rho$. The present work determines the branching ratio $BR(\omega \to \eta\gamma)$ with higher accuracy than all previous measurements.

The branching ratio $BR(\rho \to \eta\gamma)$ measured in this work is only a by-product of the coupled analysis of both channels. The error is too large for a meaningful comparison with previous experiments [6] [7]. Since all production branching ratios for $\rho$ and $\omega$ are fixed to their table values in the coupled analysis, the somewhat large branching ratio $BR(\rho \to \eta\gamma)$ could be explained by a systematically overestimated production branching ratio for $\rho$ or a systematically underestimated production branching ratio for $\omega$. Some production branching ratios (e.g. $\overline{p}p \to \eta\rho$) are not well-known or different experiments are in conflict with each other (see refs. [13] and [16] for a compilation of the available data).

An upper limit for direct decay $\omega \to 3\gamma$ has previously been published by

| author | comment | $BR$ $\omega \to \eta\gamma$ $[10^{-4}]$ | $BR$ $\rho \to \eta\gamma$ $[10^{-4}]$ | $\phi$ $[^\circ]$ | $BR$ $\omega \to 3\gamma$ $[10^{-4}]$ |
|---|---|---|---|---|---|
| this work | $\overline{p}p \to \eta\omega$ | $7.05 \pm 1.19$ | | | |
| this work | coupled fit | $6.6 \pm 1.7$ | $9.1 \pm 6.8$ | $-18^{+58}_{-27}$ | |
| this work | $\overline{p}p \to \pi^0\omega$ | | | | $< 1.9$ at 95% $CL$ |
| Andrews [6] | constructive | $3.0^{+2.5}_{-1.8}$ | $3.6 \pm 0.9$ | $-11 \pm 38$ | |
| Andrews [6] | destructive | $29 \pm 7$ | $5.4 \pm 1.1$ | $203 \pm 10$ | |
| Dolinsky [7] | constructive | $7.3 \pm 2.9$ | $4.0 \pm 1.1$ | 0 | |
| Dolinsky [7] | destructive | $35 \pm 5$ | $7.3 \pm 1.5$ | 180 | |
| Alde [5] | | $8.3 \pm 2.1$ | | | |
| Prokoshkin [19] | | | | | $< 2.0$ at 90 % $CL$ |

Table 7: *Summary of experimental results from this work and from previous measurements. The comment 'constructive/destructive' denotes the constructive/destructive interference solution. The relative phase $\phi$ was not measured by Dolinsky, but set to* $0^\circ$ *and* $180^\circ$*, respectively.*

Prokoshkin and Samoilenko [19]. Their value is of the same order, but a comparision with value measured in this work is difficult since their analysis method is not described. The present analysis yields a lower upper-limit with an even higher confidence level.

# 8 Conclusions

Antiproton-proton annihilation at rest into $\pi^0\omega$ and $\eta\omega$ was used to study radiative decays of $\omega$, particular to determine the branching ratio $BR(\omega \to \eta\gamma)$ and to search for the direct decay $\omega \to 3\gamma$. 63k $\pi^0\omega$ and 55k $\eta\omega$ events were reconstructed requiring $\omega \to 3\gamma$. The resulting Dalitz plots were analysed. The experimental results are summarized in table 8.

| measurement | analysis method | value |
|---|---|---|
| $BR(\omega \to \eta\gamma)$ | in $\eta\omega$ (assuming no contribution from $\rho$) | $(7.05 \pm 1.19) \times 10^{-4}$ |
| $BR(\omega \to \eta\gamma)$ | $\pi^0\omega$ - $\eta\omega$ coupled analysis | $(6.6 \pm 1.7) \times 10^{-4}$ |
| $BR(\rho \to \eta\gamma)$ | $\pi^0\omega$ - $\eta\omega$ coupled analysis | $(9.1 \pm 6.8) \times 10^{-4}$ |
| relative phase $\phi$ | $\pi^0\omega$ - $\eta\omega$ coupled analysis | $(-18^{+58}_{-27})^\circ$ |
| $BR(\omega \to 3\gamma)$ | in $\pi^0\omega$ | $< 1.9 \times 10^{-4}$ at 95% $CL$ |

Table 8: *Summary of experimental results.*

Two different methods were applied to extract the $\omega \to \eta\gamma$ branching ratio:

1. In $\eta\omega$, the relative contribution from $\eta\rho$ is very small. The channel was therefore assumed to be free of coherent background from $\rho$ and the $\omega \to \eta\gamma$ branching ratio was measured directly by counting the number of events in the Dalitz plot.

2. To gain information about the open problem concerning the sign of $\rho - \omega$ mixing, a coupled analysis of both $\omega$ production channel was performed. The $\rho$ contribution was simulated using Monte Carlo events.

The two measured branching ratios $BR(\omega \to \eta\gamma)$ are completely consistent thus proving that indeed the coherent contribution from $\rho$ can be neglected in $\eta\omega$.

The coupled analysis further determines the branching ratio $BR(\rho \to \eta\gamma)$, but with very large errors, and the mixing angle $\phi \approx 0$. $\rho - \omega$ mixing is therefore *constructive* in the $\eta\gamma$ system. Furthermore, no ambiguities between constructive and destructive interference were found.

In addition, an upper-limit for the direct radiative decay $\omega \to 3\gamma$ was measured in the $\pi^0\omega$ channel. It was assumed that this process is purely electromagnetic and has therefore the same dynamics as the process $e^+e^- \to 3\gamma$, where the positronium system has $J^{PC} = 1^{--}$.

The ratio of branching ratio

$$\frac{BR(\omega \to \eta\gamma)}{BR(\omega \to \pi^0\gamma)} = (8.29 \pm 1.31) \times 10^{-3} \tag{80}$$

measured in the present work is in agreement with the prediction from $SU(3)$ [5]

$$\frac{\Gamma(\omega \to \eta\gamma)}{\Gamma(\omega \to \pi^0\gamma)} = \frac{p_\eta^3}{p_{\pi^0}^3}\frac{1}{9}\cos^2\phi = 10.2 \times 10^{-3} \tag{81}$$

where $\phi \equiv 54.7^\circ + \theta$, $\theta = -17.3^\circ$ is the pseudoscalar mixing angle and $p_\pi$ and $p_\eta$ denote the decay momenta in the $\omega$ rest frame.

# A The Kinematic Fitting Method

This Appendix describes the derivation of the kinematic fit method used in the present work.

Regard the measurement of $n$ parameters $x_i$

$$\vec{x}^{\,0} \equiv (x_1^0, x_2^0, \ldots, x_n^0)^T, \tag{82}$$

where the $x_i$ are connected by $q$ constraints ($q < n$):

$$f_k(\vec{x}) = 0, \quad k = 1, \ldots, q. \tag{83}$$

The parameters are measured with certain errors $\sigma_i$, as mentionend above. The errors are gathered in the so called *error matrix*

$$G \equiv \begin{bmatrix} \sigma_1^{-2} & 0 & \cdots & 0 \\ 0 & \sigma_2^{-2} & \cdots & 0 \\ \vdots & \vdots & \ddots & \vdots \\ 0 & 0 & \cdots & \sigma_n^{-2} \end{bmatrix} \tag{84}$$

The problem may be stated to find new, corrected values $\vec{x}$ by the minimization of

$$\chi^2 \equiv \left(\vec{x}^{\,0} - \vec{x}\right)^T \cdot G \cdot \left(\vec{x}^{\,0} - \vec{x}\right) \tag{85}$$

where equation 83 must hold for the corrected values $\vec{x}$. The usually used method to incorporate constraints among the variables is by the use of *Lagrangian* multipliers. The $q$ multipliers $\alpha_i$ are gathered in a vector:

$$\vec{\alpha} \equiv (\alpha_1, \alpha_2, \ldots, \alpha_q)^T. \tag{86}$$

With the introduction of $\vec{\alpha}$, the initial $\chi^2$ function transforms into

$$L \equiv (\vec{x}^{\,0} - \vec{x})^T \cdot G \cdot (\vec{x}^{\,0} - \vec{x}) + 2\vec{\alpha}^T \vec{f}(\vec{x}), \tag{87}$$

which is the *Lagrangian* function. $\vec{f}$ is usually nonlinear in $\vec{x}$ and to solve the problem $\vec{f}$ is expanded in a Taylor series arount $\vec{x}^{\,0}$:

$$\begin{aligned} \vec{f}(\vec{x}) &\simeq \vec{c} - B \cdot (\vec{x}^{\,0} - \vec{x}) \\ &\doteq 0, \end{aligned} \tag{88}$$

where

$$B \equiv \begin{bmatrix} \partial f_1/\partial x_1 & \cdots & \partial f_1/\partial x_n \\ \vdots & & \vdots \\ \partial f_q/\partial x_1 & \cdots & \partial f_q/\partial x_n \end{bmatrix} \tag{89}$$

and

$$\vec{c} \equiv (f_1(\vec{x}^{\,0}), \ldots, f_q(\vec{x}^{\,0}))^T. \tag{90}$$

With the Taylor approximation made in equation 88, equation 87 becomes

$$L = (\vec{x}^{\,0} - \vec{x})^T G(\vec{x}^{\,0} - \vec{x}) + 2\vec{\alpha}^T(\vec{c} - B(\vec{x}^{\,0} - \vec{x})). \tag{91}$$

The $\chi^2$ with the given boundary condition is minimal if $L$ has a vanishing total derivation, i.e. if

$$\mathrm{d}L = 2(\vec{x}^{\,0} - \vec{x})^T G\ \mathrm{d}(\vec{x}^{\,0} - \vec{x}) - 2\vec{\alpha}^T B\ \mathrm{d}(\vec{x}^{\,0} - \vec{x}) = 0, \tag{92}$$

which is equivalent to

$$2(\vec{x}^{\,0} - \vec{x})^T G - 2\vec{\alpha}^T B = 0. \tag{93}$$

Transposing equation 93 leads to

$$\vec{x}^{\,0} - \vec{x} = G^{-1}B^T\vec{\alpha}. \tag{94}$$

To determine the vector $\vec{\alpha}$, one inserts this equation into equation 88 and gets

$$\vec{\alpha} = (BG^{-1}B^T)^{-1}c. \tag{95}$$

Therefore the best estimation for the real value $\vec{x}$ is given by

$$\vec{x} = \vec{x}^{\,0} - G^{-1}B^T(BG^{-1}B^T)^{-1}c. \tag{96}$$

Since $f$ generally is a non-linear function and the first order Taylor series is only an approximation to the real function, the output of equation 96, $\vec{x}^{\,1}$, only gives a first approximation to the best estimation $\vec{x}$. Equation 96 therefore has to be iterated with $\vec{x}^{\,1}$ as the new starting value. Only $B$ and $\vec{c}$ have to be evaluated again, the error matrix $G$ does not change with the proceeding iteration. The convergency criteria for the iteration is usually defined through the $\chi^2$: if the changement of $\chi^2$ is small enough the iteration is stopped and the last vector $\vec{x}^{\,l}$ from iteration step $l$ is assumed to be close to the best estimation $\vec{x}$.

# B The Normalization of 6$\gamma$ Background Channels

In this appendix, the derivation of the overall normalization constant $f$ for 6$\gamma$ MC events, used in subsection 5.1 is described. The derivation of this constant is done here with events of the type $\pi^0\pi^0\eta$, but the results are the same for $\pi^0\pi^0\pi^0$ and $\pi^0\eta\eta$.

Let us define the following quantities:

| | | |
|---|---|---|
| $N^{MC}$ | : | Number of generated Monte Carlo events of the type $\pi^0\pi^0\eta$, |
| $N^{MC}_{eff}$ | : | Number of Monte Carlo events after weighting the events, |
| $N_{\pi^0\pi^0\eta}$ | : | Number of events in the $\pi^0\pi^0\eta$ data Dalitz plot, |
| $N_{bins}$ | : | Number of bins in the $\pi^0\pi^0\eta$ data Dalitz plot, |
| $n_i$ | : | Number of entries in the bin in the $\pi^0\pi^0\eta$ data Dalitz plot in which the event $i$ falls, |
| $n_k$ | : | Number of entries in the bin $k$ in the $\pi^0\pi^0\eta$ data Dalitz plot, |
| $N^{exp}_{\pi^0\pi^0\eta}$ | : | Number of $\pi^0\pi^0\eta$ events expected in the all neutral data sample. |

The weight $w_i$ for MC event $i$ is then defined as

$$w_i \equiv n_i \cdot \frac{N_{bins}}{N_{\pi^0\pi^0\eta}}. \tag{97}$$

The effective number of MC events (i.e. the number of MC events after weighting) is given by

$$N^{MC}_{eff} = \sum_{i=1}^{N^{MC}} w_i. \tag{98}$$

To compare MC events directly to data events, the effective number of produced MC events has to be scaled to the expected number of $\pi^0\pi^0\eta$ events,

$$N^{exp}_{\pi^0\pi^0\eta} = f \cdot N^{MC}_{eff} = f \cdot \sum_{i=1}^{N^{MC}} w_i, \tag{99}$$

which defines the global normalization constant $f$. For the determination of $f$, the definition of $w_i$ is used and the sum over all MC events is calculated:

$$\begin{aligned} N^{exp}_{\pi^0\pi^0\eta} &= f \cdot \textstyle\sum_{i=1}^{N^{MC}} w_i \\ &= f \cdot \textstyle\sum_{i=1}^{N^{MC}} n_i \frac{N_{bins}}{N_{\pi^0\pi^0\eta}}. \end{aligned} \tag{100}$$

Assuming that the MC $\pi^0\pi^0\eta$ Dalitz-Plot is completely flat ($N^{MC} \gg 1$) before weighting and contains the same number of bins as the measured $\pi^0\pi^0\eta$ Dalitz plot, the sum over all MC events in eqn. 100 can be approximated by

| Event type | $N^{MC}$ | $N^{exp}$ | $f$ |
|---|---|---|---|
| $\pi^0\pi^0\pi^0, \to 6\gamma$ | 260,000 | $2,370,200 \pm 424,000$ | $9.12 \pm 1.63$ |
| $\pi^0\pi^0\eta, \to 6\gamma$ | 905,900 | $1,006,700 \pm 196,300$ | $1.06 \pm 0.22$ |
| $\pi^0\eta\eta, \to 6\gamma$ | 110,000 | $117,700 \pm 25,200$ | $1.07 \pm 0.23$ |

Table 9: *Summary of $6\gamma$ MC events. $N^{MC}$: Number of generated MC events, $N^{exp}$: Number of expected events in the all neutral data sample used in this work, $f$: scaling factor.*

$$\sum_{i=1}^{N^{MC}} n_i \simeq \sum_{k=1}^{N_{bins}} n_k \cdot \frac{N^{MC}}{N_{bins}}. \tag{101}$$

With this approximation, eqn. 100 becomes

$$\begin{aligned} N^{exp}_{\pi^0\pi^0\eta} &= f \cdot \textstyle\sum_{i=1}^{N^{MC}} n_i \frac{N_{bins}}{N_{\pi^0\pi^0\eta}} \\ &\simeq f \cdot \textstyle\sum_{k=1}^{N_{bins}} n_k \frac{N^{MC}}{N_{bins}} \frac{N_{bins}}{N_{\pi^0\pi^0\eta}} \\ &= f \cdot \frac{N_{\pi^0\pi^0\eta}}{N_{\pi^0\pi^0\eta}} N^{MC} \\ &= f \cdot N^{MC}, \end{aligned} \tag{102}$$

since $\sum_{k=1}^{N_{bins}} n_k = N_{\pi^0\pi^0\eta}$. Hence the factor $f$ is the fraction of expected and generated $\pi^0\pi^0\eta$ events,

$$f = \frac{N^{exp}_{\pi^0\pi^0\eta}}{N^{MC}}, \tag{103}$$

The total weight $W_i$ for MC event $i$ is therefore given by

$$W_i = f \cdot w_i = \frac{N^{exp}_{\pi^0\pi^0\eta}}{N^{MC}} \cdot n_i \cdot \frac{N_{bins}}{N_{\pi^0\pi^0\eta}}. \tag{104}$$

The branching ratios used to calculate the number of expected events $N^{exp}$ are [11] [12]:

$$\begin{aligned} BR(\overline{p}p \to 3\pi^0) &= (6.2 \pm 1.0) \times 10^{-3}, \\ BR(\overline{p}p \to \pi^0\pi^0\eta) &= (6.7 \pm 1.2) \times 10^{-3}, \\ BR(\overline{p}p \to \pi^0\eta\eta) &= (2.0 \pm 0.4) \times 10^{-3}, \\ BR(\eta \to \gamma\gamma) &= (38.8 \pm 0.5)\%. \end{aligned} \tag{105}$$

The branching ratio $BR(\overline{p}p \to \textit{all neutral})$ has been previously measured by the Crystal Barrel Collaboration in ref. [26]:

$$BR(\overline{p}p \to \textit{all neutral}) = (3.9 \pm 0.3)\%. \tag{106}$$

The number of expected events is therefore given by

$$N^{exp} = \frac{N^{all\ neutral}}{BR(\overline{p}p \rightarrow all\ neutral)} \cdot BR(\overline{p}p \rightarrow \left\{ \begin{array}{l} \pi^0\pi^0\pi^0 \\ \pi^0\pi^0\eta \\ \pi^0\eta\eta \end{array} \right\} \rightarrow 6\gamma), \tag{107}$$

where $N^{all\ neutral}$ denotes the number of analysed all-neutral events (see chapter 4):

$$N^{all\ neutral} = 15,457,788. \tag{108}$$

The simulated $6\gamma$ channels, the number of produced Monte Carlo events $N^{MC}$, the number of expected events in the data set and the normalization constant $f$ are summarized in table 9.

# C Errors on Weighted Histograms

The method which was used to simulate background contributions (presented in the section 5 and appendix B) requires the weighting of events. When a histogram is filled with these weighted events, the error no longer equals the square root of the bin entry but depends on the weighting constants. The statistical error on a bin in such a histogram shall be derived in this section.

Assume a bin in a histogram for which

$$N = \sum_{i=1}^{k} q_i. \tag{109}$$

The error on $N$ is then given by:

$$\sigma_N^2 = \sum_{i=1}^{k} \sigma^2(q_i). \tag{110}$$

In the case of a weighted histogram, $q_i$ has the general form

$$q_i = W_i \cdot m_i, \tag{111}$$

where $W_i$ is the weight and $m_i$ the number of entries before weighting. The error on $q_i$ is therefore:

$$\begin{aligned} \sigma_{q_i}^2 &= \left(\tfrac{\partial q_i}{\partial m_i} \cdot \sigma_{m_i}\right)^2 + \left(\tfrac{\partial q_i}{\partial W_i} \cdot \sigma_{W_i}\right)^2 \\ &= (W_i \cdot \sqrt{m_i})^2 + (m_i \cdot \sigma_{W_i})^2 \\ &= W_i^2 \cdot m_i + m_i^2 \cdot \sigma_{W_i}^2. \end{aligned} \tag{112}$$

For $m_i \equiv 1$, which is the case when every single event is weighted, eqn. 112 reduces to

$$\begin{aligned} \sigma_{q_i}^2 &= W_i^2 + \sigma_{W_i}^2 \\ &= W_i^2 \left(1 + r_{W_i}^2\right), \end{aligned} \tag{113}$$

where $r_{W_i} \equiv \sigma_{W_i}/W_i$. The error on one bin entry is therefore $W_i^2$ with a correction $(1 + r_{W_i})$ if $W_i$ itself has an error. With this relation, the error on $N$ is

$$\sigma_N^2 = \sum_{i=1}^{k} W_i^2 \left(1 + r_{W_i}^2\right). \tag{114}$$

Following the definition of $W_i$ in eqn. 104, the error on $W_i$ is $r_{W_i}^2 = r_f^2 + r_{w_i}^2$. The error on $f$ is given in tables 9 and 5, whereas the error on $w_i$ is $r_{w_i} = \sqrt{n_i}/n_i$ (see eqn. 97 for the definition of $w_i$).

# References


[1] M. Gell-Mann: A Schematic Model of Baryons and Mesons. *Phys. Lett.* **8** (1964) 214.

[2] K. Peters, E. Klempt: The suppression of $s\overline{s}$ pair creation from tensor meson decays. *Phys. Lett. B* **352** (1995) 467-471.

[3] C. Amsler and F. Close: Is $f_0(1500)$ a scalar glueball? *Phys. Rev. D* **53** (1996) 295.

[4] P.J. O'Donnell: Radiative Decays of Mesons. *Rev. Mod. Phys.* **53** (1981) 673.

[5] D. Alde *et al.*: Model-independent Measurement of $\omega \to \eta\gamma$ Branching Ratio. *Z. Phys.* **C61** (1994) 35.

[6] D.E. Andrews *et al.*: $\eta\gamma$ Decays of $\rho^0$, $\omega$ and $\phi$ Mesons. *Phys. Rev. Lett.* **38** (1977) 198-201.

[7] S.I. Dolinsky *et al.*: Radiative decays of $\rho$ and $\omega$ mesons. *Z. Phys* **C42** (1989) 511-518.

[8] E. Aker *et al.*: The Crystal Barrel, Proposal. CERN/PSCC/85-56, 11 October, 1985.

[9] Crystal Barrel Collaboration, E. Aker *et al.*: The Crystal Barrel spectrometer at LEAR. *Nucl. Instrum. Methods* **A321** (1992) 69-108.

[10] S. Brandt: Datenanalyse. Bibliographisches Institut, Mannheim 1981.

[11] Particle Data Group: Review of Particle Properties. *Phys. Rev. D* **50** (1194) 1.

[12] Crystal Barrel Collaboration, C. Amsler *et al.*: Coupled channel analysis of $\overline{p}p$ annihilation into $\pi^0\pi^0\pi^0$, $\pi^0\pi^0\eta$ and $\pi^0\eta\eta$. *Physics Letters* **B 355** (1995) 425.

[13] Crystal Barrel Collaboration, C. Amsler *et al.*: Antiproton-proton annihilation at rest into two-body final states. *Z. Phys.* **C 58** (1993) 175-189.

[14] C. Amsler, J.C.Bizot: Simulation of Angular Distributions and Correlations in the Decay of Particles with Spin. *Com. Phys. Comm.* **30** (1983) 21-30.

[15] C. Strassburger: $S$- and $P$-wave contributions in $\pi^0\omega$ and $\eta\omega$ final states, Crystal Barrel internal note.

[16] C. Amsler and F. Myhrer: Low Energy Antiproton Physics. *Annu Rev. Nucl. Part. Sci.* **41** (1991) 219-267.

[17] M. Deutsch: Annihilation of Positrons. *Progr. Nucl. Phys.* **3** 131.

[18] A. Ore, L. Powell: Three-Photon Annihilation of an Electron-Positron Pair. *Phys. Rev.* **75** (1949) 1696.

[19] Yu. D. Prokoshkin and V. D. Samoilenko: Experimental Evidence for a Rare Radiation Decay $\omega \to \pi^0\pi^0\gamma$. *Physics - Doklady* **40** (1995) 273-275.

[20] S. Coleman and S. Glashow: Departures from the Eightfold Way: Theory of Strong Interaction Breakdown. *Phys. Rev.* **134** (1964) B671-B681.

[21] S. Goldhaber *et al.*: Theory of $\rho-\omega$ Interference in $\pi^+\pi^-$ Production. *Physics Letters* **30B** (1969) 249.

[22] H.B. O'Connell *et al.*: Rho-omega mixing, vector meson dominance and the pion form-factor. HEP-PH/9501251.

[23] M.J. Iqbal *et al.*: Mesonic Width Effects on the Momentum Dependence of the $\rho - \omega$ Mixing Matrix Element. NUCL-TH/9504026, submitted to *Phys. Rev. Lett.*

[24] N.N. Achasov, G.N. Shestakov: *Elem. Chast. At. Jadra* **9** (1978) 48.

[25] B. Armenteros, B. French, in *High Energy Physics*, ed. E. H. S. Burhop. London: Academic **4** (1969) 237.

[26] Crystal Barrel Collaboration, C. Amsler *et al.*: Antiproton-proton annihilation at rest into $\omega\pi^0\pi^0$. *Physics Letters* **B 311** (1993) 362-370.